Nanoscale characterisation of crystal zoning

Nanoscale characterisation of crystal zoning

Kate Saunders[1*], Ben Buse[1], Matt R Kilburn[2], Stuart Kearns[1], Jon Blundy[1].

[1]School of Earth Sciences, University of Bristol, Wills Memorial Building, Queens Road, Bristol, BS8 1RJ, UK.

[2]Centre for Microscopy, Characterisation and Analysis & ARC Centre of Excellence for Core to Crust Fluid Systems, The University of Western Australia, 35 Stirling Highway, Crawley WA 6009, Australia

*Now at: School of Geosciences, University of Edinburgh, Grants Institute, Kings Building, West Mains Road, EH9 3JW, UK.

Corresponding author: Kate Saunders

E-mail: Kate.Saunders@ed.ac.uk

Telephone: +44 (0)131 650 2544

Fax: +44 (0)131 669 3184

Highlights

- Application of low kV FEG-EPMA and NanoSIMS to zoned crystals.
- NanoSIMS attained relative chemical profiles on a nanoscale spatial resolution.
- Quantitative nanoscale spatial resolution achieved by low kV FEG- EPMA

Abstract

Advances in analytical techniques are fundamental to the enhanced understandings of many geological processes. Zoned volcanic crystals have been analysed by low (5) kV field emission gun electron probe micro-analyser (FEG-EPMA) and NanoSIMS to obtain sub-micrometre chemical profiles and compared to time-of-flight SIMS (TOF-SIMS) and high (15-20) kV EPMA profiles. Plagioclase and orthopyroxene crystals have been analysed by FEG-EPMA, at accelerating voltages of 5 kV providing a spatial resolution (step size) of ≤. 350 nm (the resolution of the lowest energy X-ray) for orthopyroxene crystals using a 30 nm beam and ca. 750 nm for plagioclase crystals which at low voltages are unstable and require a 500 nm defocused beam. Step sizes are comparable in size to interaction volumes. Analytical protocols are detailed that permit quantitative major and minor element compositions to be acquired at similar precision and accuracy as traditional EPMA analyses at 15-20 kV. NanoSIMS analysis of the same crystals provides a greater spatial resolution of up to 200 nm and allows the measurement of Li also. The NanoSIMS profiles, however, cannot currently be quantified. The ability to analyse crystals at sub-micrometre scales is demonstrated by the good agreement between NanoSIMS, FEG-EPMA, conventional EPMA and TOF-SIMS data. FEG-EPMA, NanoSIMS and TOF-SIMS techniques have broad applications within the earth sciences. In petrologic studies for example, these methods have the ability to analyse small crystals in experimental charges and provide chemical profiles of crystal zoning at a spatial resolution of ca. 200-300 nm. Such profiles are important in crystal forensics and diffusion chronometry studies. The implications for the latter application are that timescales of volcanic processes that occur in the days-years immediately prior to the eruption can now be studied.

Keywords: FEG-EPMA, NanoSIMS, crystal zoning, diffusion chronometry

1. Introduction

Fundamental to our understanding of volcanic eruptions are the timescales over which magmatic processes occur in the lead up to eruption. The evolution of a magmatic system may occur over millennia (e.g. Charlier et al., 2005; 2008; Claiborne et al., 2010), whilst the final stages of magma evolution may occur over much shorter timescales immediately prior to eruption (e.g. Morgan et al., 2004; Martin et al., 2008; Kahl et al., 2011;Druitt et al., 2012; Saunders et al., 2010, 2012a). Many conventional radiometric dating techniques do not have the resolution to interrogate timescales of magmatic processes that occur in the days-years immediately prior to eruption, as the half-lives of elements are greater than the time scales of interest. An alternative method and one that is increasingly used in volcanic studies is diffusion chronometry (e.g. Costa et al., 2003, 2008; Morgan et al., 2006; Druitt et al., 2012; Saunders et al., 2012a), which uses the diffusive relaxation of chemical zoning in igneous crystals to retrieve timescales of magmatic processes. Different elements have the potential to record different magmatic processes such that by studying several different elements within a crystal it is possible to gain insights into several different components of the magma genesis. Conversely, because different elements diffuse through crystals at different rates their diffusive relaxation can be used to extract timescales from minutes to millennia. The chemical zonation of minerals that provide the basis of diffusion chronometry can vary from 10's of micrometres to less than a few nanometres.

Diffusion serves to modify the elemental concentration of adjacent crystal zones as crystals attempts to obtain equilibrium internally and with the external melt. On eruption, diffusion effectively ceases due to rapid decrease in temperature (quenching). However, the timescales that can be calculated using diffusional methods are limited by the diffusivity of the element of interest and resolution of the measured chemical profile that is dependent on the analytical methods employed to obtain the profile. The rate of diffusion depends on the chemical potential gradient and the diffusion coefficient at the conditions of interest. Diffusion coefficients are specific to the mineral and element of interest. If the characteristic diffusion length is shorter than the analytical length scale, no temporal information can be obtained. To avoid complications from convolution and overlapping analyses, four analytical points clear of the adjacent background chemical composition on either side of the chemical profile are required to extract diffusion profiles that can be modelled (Costa and Morgan, 2010). Thus in order to investigate timescales that occur in days-months prior to eruption, for all but the most rapidly diffusing elements, sub-micrometre spatial resolution is required.

Recent studies have exploited the high-resolution of backscattered electron (BSE) images and cathodoluminescence images (Morgan et al., 2004; Wark et al., 2007; Saunders et al., 2010, 2012a) to increase the spatial resolution of chemical profiles for diffusion studies. The intensity of the images reflects specific aspects of the chemical composition of the crystal. Thus, the intensity of each pixel can be used as a proxy for the chemical composition at a spatial resolution of 200-400 nm (Saunders et al., 2012 a & b). This technique, however, is limited to a few specific elements that due to their atomic structure are disproportionately represented in BSE images (Reed, 1996).

These may be major elements of a solid solution or elements with high atomic number relative to their crystal matrix. For example, BSE images of pyroxene crystals display information predominantly on the Fe-Mg content of the crystal (e.g. Morgan et al., 2004; Saunders et al., 2012b). As the BSE images cannot be used to obtain any information on the chemical gradient of any other minor or trace elements across interfaces within crystals, an alternative analytical technique is required if other elements are to be modelled. Ideally these techniques would allow quantification of the composition. However, diffusion modelling relies on a concentration gradient without the need for absolute concentration; this allows us to exploit analytical techniques that can only achieve a relative concentration profile, even though the long-standing problem of quantification remains.

In the last few years, several techniques have emerged that can potentially obtain chemical profiles at the nanoscale (used to describe sub-micrometre resolution). These include NanoSIMS, field emission gun (FEG)-EPMA and time-of-flight (TOF) SIMS (see Saunders et al., 2012b). Depth profiling with a conventional SIMS also has the ability to achieve a 100 nm spatial resolution (Genareau et al., 2007), although it requires very careful crystal orientation during analysis such that the chemical profile is exactly perpendicular to the interface of interest. As the location (depth) and shape of this interface may not be known, obtained profiles may not be perpendicular. Consequently, any chemical profile obtained may be artificially lengthened resulting in overestimation of any calculated timescale (Costa and Morgan, 2010), whereas EPMA, NanoSIMS and TOF-SIMS allows us to observe the crystal zonation in 2D prior to analysis, allowing the most vertical boundaries to be chosen for analyis and to perform complementary analyses.

1.1 Developments in EPMA

Since the 1960's the EPMA has been routinely used to determine the chemical composition of minerals on a micrometre scale. Typical operating conditions for mineral analyses are an accelerating voltage of 15-20kV and a beam current of 5-20 nA. Thus, the approximate spatial resolution attainable is 2-3 μm for a silicate mineral with a density of ca. 2700 kg/m^3 (Figure 1). The spatial resolution is governed by the interaction volume (the volume in which beam electrons interact with the sample to produce secondary radiation) with most x-rays analysed having a large overvoltage (ratio of beam energy to critical excitation energy, typically <2) and generated from a large fraction of the total interaction volume (Goldstein et al., 1992). The interaction volume is therefore used as an approximation of the total spatial resolution In situations where particular elements for which the x-ray analysed has a small overvoltage (e.g. Ca K at 5 kV, overvoltage 1.2) the actual spatial resolution will be much smaller. This results from beam electrons losing energy as they penetrate into the sample restricting the x-rays which they can excite (Figure 1).

Reducing the spatial resolution is possible by decreasing the accelerating voltage which in turn decreases the interaction volume by reducing the beam penetration (Merlet and Llovet 2012); however, this also increases the beam spot size thus offsetting any improvement in resolution. At low accelerating voltages and modest beam currents (5-20 nA) using a tungsten or LaB_6 sourced EPMA the large increase in spot size with decreasing accelerating voltage limits the lateral resolution to a minimum of about 1 μm at 10 kV for silicate minerals. Using a FEG source the primary beam intensity is much higher and the increase in beam size constrained to tens of nanometres (McSwiggen 2013). As the X-ray generation is significantly reduced at low accelerating potentials it is necessary to increase beam currents to give

a sufficient count rate. The rise in beam currents further reduces lateral spatial resolution. Even so, the instrument specification for a JEOL 8530 FEG-EPMA is that the spot size will be no more than 100nm at 10kV with a beam current of 100nA

Figure 1

With these advances, the FEG-EPMA is well facilitated to allow the quantitative chemical analysis of nanoscale volumes of material. A Monte Carlo simulation (figure 1) predicts that at an accelerating voltage of 5 kV and a beam current of 10 nA, a spot size of about 30nm (smallest observable feature measured in SE) will yield a spatial resolution of ca. 350 nm ; considerably smaller than at higher accelerating voltages.

1.2 Developments in in-situ mass spectrometry techniques

With advances in the last 30 years, in-situ mass spectrometry techniques have allowed the analysis of trace elements in crystals and melt inclusions. Two widely used, in-situ mass spectrometry methods are laser ablation inductively coupled plasma mass spectrometry (LA-ICPMS) and secondary ion mass spectrometry (SIMS). Spot analyses of trace elements in plagioclase and pyroxene crystals are limited to a diameter of 6-20 μm (Berlo et al., 2007; Kent et al., 2007) in order to achieve sufficient precision and accuracy of analyses. Alternative methods such as NanoSIMS and TOF-SIMS (see Saunders et al., 2012b) have yet to be fully exploited in the geological sciences as the protocols for quantification have not yet been routinely established.

Plagioclase and orthopyroxene crystals from the 1980 Mount St. Helens (MSH) eruptions have been analysed to demonstrate the potential of these two new

techniques for diffusion chronometry. Four plagioclase crystals from four 1980 MSH eruptions are characterised for Li, Mg, Si, K and Ca by NanoSIMS, and for major and trace elements by FEG-EPMA. One of these crystals was previously characterised by EPMA and SIMS by Berlo et al. (2007). Two orthopyroxene crystals previously characterised by TOF-SIMS and EPMA (Saunders et al., 2012b) are further characterised by FEG-EPMA here.

2. Samples and conventional SEM and EPMA techniques

Plagioclase crystals are mounted as one-inch epoxy mounts and orthopyroxene crystals as polished sections. Prior to FEG-EPMA, NanoSIMS or TOF-SIMS analyses, crystals were characterised through conventional scanning electron microscopy (SEM) and EPMA techniques.

High-resolution BSE images of crystals were collected using a tungsten-sourced Hitachi S3500-N SEM at an accelerating voltage of 20 kV at a typical image resolution of 1280 x 960 pixels. This allowed us to characterise the textural features of crystals. BSE images of crystals can then be calibrated for anorthite (*An*) composition (calculated as molar Ca/(Ca+Na+K)) or Mg # (molar Mg/(Mg+Fe^{2+}) for plagioclase and orthopyroxene respectively. The open-source software ImageJ (Abramoff et al. 2004) was used to extract the greyscale intensity of the crystal from the BSE image at the point of the EPMA analysis spot. This can then be plotted against the measured *An* composition or Mg# concentration of the crystal for plagioclase and pyroxene respectively to calibrate the whole crystal at a spatial resolution of 200-400 nm (e.g. Ginibre et al., 2002; Humphreys et al., 2008)

The distribution of elements across the crystals were analysed for two plagioclase crystals (May and August) using a conventional, tungsten-sourced 5-WD spectrometer Cameca SX-100 EPMA at the University of Bristol, with an accelerating voltage of 20 kV and 20 nA beam current focussed to give a 1 μm spot size, which for a labradorite plagioclase crystal equates to an interaction volume of ca. 2 μm^3 (Figure 1). Peak count times of 60 seconds for Ca, Al, Ti, Fe and Mg, 30 seconds for Si, K, and 20 seconds for Na. Spectrometers are set to analyse K, Na and Si first. Primary calibrations used a mixture of synthetic and natural standards and secondary standards of Kakanui kaersutite (KK1) (Jarosewich et al. 1980) and diopside.

Major element data for all crystals by EPMA and/or FEG-EPMA are presented in the Supplementary data. In addition to numerical data, secondary ion images and BSE images of each analysis area were also acquired prior to NanoSIMS analysis and FEG-EPMA analyses respectively. This allowed the location of inclusions, crystal zoning and previous analyses to be precisely located (Figure 2b). Oscillatory zonation is observed in all plagioclase crystals, with May and July samples exhibiting a sieved core. Anorthite concentrations vary from An_{35} to An_{70}. Zoning within the orthopyroxene crystals is much simpler. Mg-rich cores are mantled by Fe-rich rims with Mg# ranging between 0.64-0.69.

3. Field emission gun electron probe micro-analyser (FEG-EPMA)

Orthopyroxene and plagioclase crystals were analysed on a JEOL 8530F FEG-EPMA at the University of Bristol, using an accelerating voltage of 5 kV and 10 nA beam current for major elements and 100-200 nA for minor and trace elements. Two forms of analysis are considered: firstly lines of quantitative spot analyses to produce quantitative element profiles; and secondly qualitative line scans consisting of peak x-

ray intensities collected continuously along a profile. Primary calibrations for FEG-EPMA used the same mixture of synthetic and natural standards as were used with the conventional EPMA.

3.1 Quantitative spot analyses

The plagioclase crystals are labradorite in composition, which is approximately midway between the end-members albite ($NaAlSi_3O_8$) and anorthite ($CaAl_2Si_2O_8$) within which plagioclase forms a solid solution. Labradorite is generally regarded to be relatively stable under the electron beam unlike the albite end-member which suffers beam damage during conventional (15-20kV) EPMA analysis. At 5 kV accelerating voltage, the interaction volume can be reduced to ca. 350 nm^3 (Figure 1) with a focused beam (diameter ca. 30 nm, at a 10 nA beam current. At these conditions, however, beam damage is exacerbated and even labradorite experiences appreciable sample heating and Na loss. To mitigate this, the beam is defocused to ca. 500 nm during plagioclase analyses, reducing the power input per cubic nm and the surface temperature rise. This degrades the lateral resolution to ca. 750 nm, which is similar to the minimum step spacing ($\geq$ 650 nm) that can be utilised to prevent each subsequent analysis being affected by beam damage inflicted by the previous analysis (beam damage propagation). At these conditions K also migrates but to a lesser extent and requires count times of < 25 seconds, restricting the detection limits and accuracy achievable for K.

A second consequence of low voltage EPMA is that any contamination layer that builds up on the surface will become a significant proportion of the excitation volume. This is time dependent and will result in a fractional intensity loss that is a function of the electron energy loss due to the layer and increased X-ray absorption

(Reed 1996). For the X-ray energies analysed here increased absorption has a negligible effect whilst electron energy loss within the contamination layer effectively reduces the landing energy on the sample – this is particularly important for the generation of low overvoltage X-rays (e.g. Ca at 5 kV, overvoltage of 1.2). In analyses of plagioclase this effect is observed as a reduction in calcium K-alpha intensity with time. To mitigate the effect, count times for those elements with a low overvoltage are reduced to a minimum. Thus, peak count times for major element plagioclase analyses are 25 seconds for K, 10 seconds for Si, Al, 5 seconds for Ca and 3 seconds for Na to mitigate loss during analysis. Trace element (Mg, Fe, Sr) analyses were performed at 200 nA with a 750 nm beam and a 3 μm spacing in order to obtain reproducible results at lower concentrations (< 100 ppm). At these conditions the plagioclase is heavily damaged and the large spacing is required to avoid previously damaged areas. This damage and any possible carbon contamination has a negligible affect on the analyses in view of the large errors involved (Table 1). Mg and Sr were analysed simultaneously on two spectrometers. Total peak count times are 900 seconds for Mg and Sr and 450 seconds for Fe. Sr was analysed using two PET crystals with only the upper background measured and a flat background slope avoiding interference from the Si K-beta satellite peak. In addition, Si, Ca, Na and Al were analysed simultaneously on the EDS, allowing for major and trace element profiles to be correlated efficiently.

Table 1

The requirement to use different beam currents means major and trace element analyses cannot be obtained simultaneously and the small shift (ca. 3 μm) in beam alignment with a large change in beam current requires the major and trace profiles to be positioned separately. This creates problems in ensuring the lines are perfectly

parallel to each other and in the positioning of the lines for it is not always possible to perform analysis adjacent to one another, as previous chemical analyses can cause beam damage to the adjacent part of the sample that modifies the composition of any subsequent analyses. Thus, some mismatch between profiles and offsetting of lines is inevitable. The major compositions are required to quantify the trace elements to correct the X-ray intensities for matrix effects, here using the ZAF correction procedure. The matrix effects are small for these elements and small discrepancies in the assigned major composition have a negligible effect when quantifying these elements at trace concentrations. For simplification a single major composition was used across all plagioclase zones (Figure 3).

Figure 3

Mg, Fe, Al and Ca analyses of orthopyroxene crystals were performed with a focused beam in view of the stability of pyroxene with ca. 300 nm step spacing to prevent analysis overlap at the conditions described above. Mg and Ca were analysed with a 10 nA beam whilst Al and Fe were analysed with a 100 nA beam in view of their lower count rate and stability. Peak count times were 10 seconds for Mg, Al, Ca, and Fe. Count times for Ca are again limited to minimise intensity loss through contamination build-up. Analyses were repeated with a 1 μm defocussed beam and 2 μm step spacing, similar to conventional EPMA set-up to ensure reproducibility of analyses at the nanoscale (Figure 4; supplementary data).

Fe was analysed using the L line x-rays which are strongly affected by chemical bonding and self-absorption (Armstrong & Crispin 2012) and poorly accounted for by standard matrix correction procedures. To correct for these affects a calibration curve

of experimental data of pyroxenes of a similar compositional range at the same kV was used to modify the Fe k-ratios.

Figure 4

3.2 Qualitative line analyses

An alternative approach removing the spacing between points and thus improve the resolution along a profile are line scans in which the stage moves continuously across a profile and the x-ray intensities are summed over a specified step size (e.g. Figure 5). These are qualitative only and whilst overlapping analyses cannot be prevented, the analytical resolution can be considered as the interaction volume from which the majority (ca. 90-98%) of x-rays are derived. The choice of step size is a balance between resolution and achieving a reasonable number of a counts per step for the given dwell time (time taken to scan across the distance of the step) and beam current. A 100nm spacing is used for the pyroxene analyses whereas for the plagioclase analyses a minimum spacing of 300 nm is required to mitigate beam damage. Analyses are performed at the same accelerating voltage and current as described for quantitative analyses above. A focused beam can be used for both plagioclase and pyroxene as the beam is rastered in a single direction perpendicular to the direction of the line scan by ± 2 μm. This mitigates beam damage and contamination and achieves a high spatial resolution parallel to the line. Line scans for pyroxene consisted of 4 accumulations, where the x-ray intensities are summed from 4 consecutive line scans over the particular profile with each accumulation having a 3 second dwell time giving a total dwell time of 12 seconds limited by loss of Ca X-rays. Line scans for plagioclase consisted of a single accumulation with a 12 second dwell time limited by Na loss. Although the line scans yield data that are qualitative count rates only, these

can be calibrated with spot analyses to affirm the true composition along the line. Line scans and spot analyses reproduce the same chemical trends (Figure 5); the observed differences resulting in non-parallel adjacent profiles are due to changes in chemistry along the interface of interest. Figure 5

3.3 Orthopyroxene FEG-EPMA versus TOF-SIMS

TOF-SIMS and EPMA analyses for two orthopyroxene crystals from the 14th May 1982 dome eruption of MSH were published previously by Saunders et al. (2012a), with new FEG-EPMA analyses for MgO, FeO, Al_2O_3, CaO for the same crystals are presented here (Figure 6). The same chemical trends are observed in both TOF-SIMS and FEG-EPMA analyses. FEG-EPMA can achieve a greater spatial resolution of 300 nm, as TOF-SIMS analyses are restricted by the 500 nm beam diameter. However, TOF-SIMS can analyse light elements such as Li and can also analyse Ti, which at 5kV with FEG-EPMA is impossible due to the L-line x-rays overlapping with O. Ti K-lines could be analysed at a higher accelerating voltage, although with the introduction of different protocols at variable voltages, each new profile adds more complexity to the processing and correlation of numerous adjacent profiles, each at different spatial resolutions. The misalignment between TOF-SIMS and FEG-EPMA arise from either the non-parallel alignment of adjacent analyses or changes in crystal chemistry along the interface. Each profile is performed perpendicular to the interface of interest, however interfaces are not perfectly planar, so some variation is inevitable.

Figure 6

4. NanoSIMS

NanoSIMS uses a high-energy Cs^+ or O^- primary ion beam to sputter the topmost atomic layers of a sample surface. Ejected secondary ions are then separated according to their mass and analysed. This has the advantage of being able to analyse a wide range of elements at spatial resolutions of down to 50 nm and produce high-resolution chemical images. The multicollection capability allows up to seven elements/isotopes to be measured simultaneously, which can speed up the analysis time compared to single detector systems where the magnet is cycled through all the desired elements one at a time. SIMS allows the analysis of light elements, such as Li, which are not possible with EPMA. Detection limits are typically much lower than EPMA (ppb for some elements), although quantification is problematic due to the differences in the secondary ion yields of different elements and between different matrices. FEG-EPMA and NanoSIMS profiles for major, minor and trace elements with a sub-micrometre spatial resolution are reported for zoned plagioclase and orthopyroxene crystals.

Plagioclase grain mounts were coated with a 10 nm layer of gold and analysed on the CAMECA NanoSIMS 50 at The University of Western Australia. Images and line scans of four plagioclase crystals were acquired using the O^- primary beam, with the mass spectrometer tuned to detect simultaneously $^{7}Li^+$, $^{24}Mg^+$, $^{28}Si^+$, $^{39}K^+$, and $^{44}Ca^+$ secondary ions. Mg, Si, K and Ca were chosen to cross-check against the EPMA data. Lithium is known to diffuse rapidly in plagioclase (Gilletti and Shanagan, 1997), and previous work on these samples from Mount St. Helens has shown that Li variations are observed in plagioclase, pyroxene and amphibole crystals (Berlo et al., 2004; Kent et al., 2007; Rowe et al., 2008). All five secondary ion species have very high

ionisation efficiencies, allowing high sensitivity even when the concentration is low and the spot size is small (i.e. at high lateral resolution). No significant interferences were present on any of masses analysed.

Four types of line scans were acquired, each focusing in more detail of the interface of interest: For coarse scans across a large area, a 200 pA (~1 μm diameter) beam was held stationary while the stage moved in 1 μm steps beneath. At each point, the beam was held in position for 15 s, but signal was only recorded from the last 5 s. This had the effect of implanting the primary O^- ion into the surface to a sufficient dose at which a steady-state of secondary ion generation was achieved (presputtering).

Medium line scans were performed by imaging an area of 50 μm at a resolution of 256 x 256 pixels (pixel size 195 nm). A line was marked on the image using the software, and at each point a small 3 x 3 pixel scan was performed around the central pixel, such that each point corresponded to an area of 586 x 586 nm. A ~ 35 pA beam with a diameter of ca. 600 nm gave an effective scan width of ca. 1 μm. The count time was 400 ms/pixel, giving 3.6 s per point, with an initial 7.2 s presputter prior to recording the signal. Fine-scale line scans were acquired with consecutively increasing lateral resolution.

Fine line scan were performed in a similar manner, but with a smaller primary beam (ca. 200 nm, ca.4 pA) giving an effective scan width of ca. 600 nm. The count time was 250 ms/pixel, giving 2.25 s per point, with an initial 2.25 s presputter per point.

The finest-scale line scan was similar again, but this time without scanning the beam, giving an effective lateral resolution of ca. 200 nm, equal to beam diameter. The count time was 5 s per point with a 5 s presputter. In the medium and fine line scans, where a scanning beam was used, each point overlapped the previous point by two-

thirds. In the finest line scan, the overlap was insignificant as the pixel size and the beam size are essentially the same. Each line scan was superimposed on the previous one, giving rise to successively deeper and thinner trenches, which in turn leads to a 'cleaner' signal as each scan is better implanted by the primary beam, free of surface contaminants, and relatively distant to the edge of the previous trench. The smallest beam diameter achievable with O- is approximately 150-200 nm, but at this size the beam rapidly digs a steep-sided crater, so count times were optimised to avoid the onset of crater edge effects.

Data were corrected for 44 ns deadtime, and expressed as cumulative counts at each point measured for each secondary ion species. To remove potential tuning artefacts, such as variations in the primary beam current or secondary ion transmission (Hinton, 1995), each measurement was normalised to the ^{28}Si signal, although this changed the profile little (Figure 7).

Figure 7

NanoSIMS data is reported as element x/Si, corrected for variation in local anorthite concentration similar to that described by Charlier et al (2012). Anorthite was calculated from the Ca/Si analysis of the NanoSIMS transverse by cross calibration to the anorthite profile obtained by the EPMA, allowing for the calculation of X_{An} for each point.

While quantification of secondary ion yields is possible with SIMS, it is extremely complicated as the ionisation probability varies for each element in different matrices and thus the relative peak intensities do not necessarily reflect the species concentrations. Thus, well-characterised, matrix-matched standards are required to

calibrate signal intensities to absolute elemental concentrations. The propagation of multiple uncertainties can results in large associated error terms. However, the *relative* intensity of an isotope does provide an accurate expression of the relative isotopic abundance in the sample (McPhail, 2006), provided there is no significant change in matrix. Thus, the relative concentration gradient of elements across compositional interfaces within the crystal can be obtained through NanoSIMS analyses without the need to determine absolute concentrations. Targeted elements must simply be present in sufficient concentrations (10's to 1000's ppm) that adequate precision can be attained along the profile on the nanoSIMS, but also that the element's diffusivities are constrained sufficiently well to permit subsequent diffusional modelling.

NanoSIMS line profiles were performed parallel to EPMA and/or previous SIMS analyses. Chemical profiles from all these methods were cross-calibrated to verify that the elemental profiles obtained by NanoSIMS and FEG-EPMA reflect the genuine variation in elemental concentrations (Figure 8, Supplementary figures 1-3). The profiles were carefully correlated spatially, by using distinct features of the chemical gradients. It should be noted that adjacent chemical profiles are not expected to mimic each other exactly due to variation in crystal chemistry along a boundary and the geometric misalignment of parallel lines between different analysis types. Coarse NanoSIMS line scans are used to locate the medium, fine and detailed line scans within the crystal. Medium line scans are often the most useful, as they extend a sufficient distance from the boundary at a spatial resolution of 600 nm.

Figure 8

A good correlation exists between Ca/Si, Mg/Si K/Si of Cameca EPMA and FEG-EPMA profiles and NanoSIMS profiles for all plagioclase crystals (Figure 8 and Supplementary Figures 1-3). Some variation is observed for K/Si in June sample (Supplementary Figure 1) between the NanoSIMS and FEG-EPMA, but this is due to the disparity in crystal chemistry along the measured interface and the fact that the error for K at 5 kV using FEG-EPMA is large, as X-ray generation for K is low given the small overvoltage of 1.39 compared to a desired value of >2 for efficient X-ray generation and long count times are prohibited by K ion migration. Mg is a trace element in plagioclase with concentrations at the detection limits of conventional EPMA techniques. However, a good correlation exists between Mg/Si profiles of EPMA and NanoSIMS (conducted on the May and August samples) and of FEG-EPMA and NanoSIMS (conducted on the June and July crystals). Li profiles analysed by both NanoSIMS and SIMS correlate well considering the difference in spatial resolution, indicating NanoSIMS can be used to analysed Li profiles at a sub-micron scale (Supplementary Figure 1). FEG-EPMA and SIMS Sr profiles correlate well for their profile shape (Figure 9), although there is a discrepancy in absolute concentrations. The reason for this is unclear and may be due to several reasons including; (i) systematic analytical error during FEG-EPMA such as contamination or beam damage; (ii) low Sr concentrations in the sample thus error brackets are large for FEG-EPMA but smaller for SIMS; (iii) the plagioclase standard used is characterised for major element concentrations at micrometre resolution, thus the standard may not be suitable for trace elements at nanoscale resolution; (iv) analyses may have occurred at different positions along the interface. Further protocol development is on-going to achieve better reproducibility of absolute Sr

concentrations by FEG-EPMA, a key component is the provision of well characterised standards with known trace element compositions.

Figure 9

The good correlation with FEG-EPMA demonstrated that the relative elemental profiles obtained on the NanoSIMS provide an accurate representation of the elemental concentrations across compositional interfaces within plagioclase crystals for Li, Mg, Ca, Si and K. The profiles demonstrate that NanoSIMS and FEG-EPMA techniques can be used to study compositional interfaces at a scale of a few hundred nanometres. For example, the analysed interface of the May sample (Figure 8) is observed to have a width of 1.57 μm with six discrete analytical points when analysed by a detailed NanoSIMS profile. A line profile by FEG-EPMA across the same interface indicates the interface boundary is 750nm wide, with nine discrete points. Conversely, traditional EPMA analyses would not be able to analyse this interface without analysing material from the adjacent crystal zones, resulting in the artificial stretching of the interface.

4. Discussion

4.1 Applications to diffusion chronometry and petrology

It is now possible, using one or a combination of the techniques described here, to obtain chemical profiles of zoned minerals with nanoscale precision. This enables diffusion chronometry studies of volcanic minerals, given knowledge of the diffusion coefficients for the relevant elements, to access time information that occurs in hours-

months prior to eruption to be probed. For example, the rim of the orthopyroxene in Figure 10 was modelled by Saunders et al. (2012b) to indicate that the rim grew 0.11 years prior to eruption, assuming a magmatic temperature of 880°C and the Fe-Mg diffusion coefficients of Ganguly and Tazzoli, (1994). The greyscale intensity of the BSE image was used as a proxy for Fe-Mg composition and gives a spatial resolution of 113 nm At 20 kV the spatial resolution of EPMA analyses is 1.9 μm which is insufficient to accurately model this interface (Figure 10). Spot analyses by FEG-EPMA at 5 kV increases the spatial resolution that can be achieved, but with a defocused beam still lacks sufficient points across the profile to accurately model this example (Figure 10). The increase in spatial resolution of the FEG-EPMA line analysis (ca. 100 nm) is sufficient to allow for diffusion modelling, although as Mg and Fe were analysed on separate profiles it is not possible to combine them into a single Fe-Mg profile. Thus, to allow direct comparison with the timescale calculated from the greyscale intensity of the BSE image, it has been assumed that the measured Fe profile represents the same profile as the Fe-Mg profile would if the Fe and Mg data were combined. The absolute concentrations are not required as diffusion chronometry relies on concentration gradients, so for this illustration this assumption should be valid. Using the same diffusion model adapted for orthopyroxene of Morgan et al. (2004), at 880 °C and diffusion coefficients of Ganguly and Tazzoli (1994) the calculated timescale is 0.109 years, within error of the timescale calculated from the BSE image. The largest errors on diffusion timescales result from the uncertainty in magmatic temperatures (e.g. Saunders et al., 2012a). Propagating a 20 °C uncertainty in magmatic temperature onto the calculated timescale result in an error of ± 18 days; hence both the FEG-EPMA and BSE image derived timescales are within error of each other. The advantage of the FEG-EPMA is the ability to attain

quantitative compositions and the analysis of other elements at the same spatial resolution as the Fe and Mg profiles. However, further refinement of the analytical protocol is required to gain all elements of interest simultaneously, for example Ti. The Ti profile in pyroxene could be used to determine the geometry of the initial profile, due to slow diffusion of Ti in pyroxene (Cherniak & Liang, 2012). However, at an accelerating voltage of 5 kV, Ti cannot be measured as the critical excitation of Ti K is 4.967 kV and the Ti L-line x-rays overlap with O. Thus for orthopyroxene analyses to include Ti, a higher accelerating voltage would be required limiting the achievable spatial resolution.

The ability to analyses multiple elements within plagioclase crystals at nanoscale resolution with the FEG-EPMA results in the potential for diffusion timescales at even shorter timescales to be calculated than can currently be accessed (Table 2). This will allow for magmatic processes much closer to the time of eruption to be investigated, expanding our knowledge of magma evolution in the lead up to a volcanic eruption.

Table 2.

Figure 10

One of the major assumptions in diffusion chronometry studies is the initial boundary condition. Simple one-dimensional diffusion models (e.g. Morgan et al. 2004) often assume a boundary that is a step function, thus any calculated timescales in these cases are maxima. This accuracy of this assumption is often questioned. Conventional microbeam techniques such as, high 15-20 kV EPMA broaden such interfaces due to

the minimum spacing of analyses spots to avoid convolution and cannot characterise the "sharpness" of the boundary (Figure 10 & 11a). The increased spatial resolution of FEG-EPMA, NanoSIMS, BSE imaging and to a lesser extent TOF-SIMS permits mineral interfaces to be analysed on length scales of several hundred nanometres (Figure 8, 10 and 11a). This reveals that some internal mineral boundaries are relatively abrupt and have shorter lengthscales than previous chemical analyses may have shown. For example, the high-resolution Ca profile by the NanoSIMS, across the plagioclase boundary of figure 8, illustrates the boundary is 1. 57 μm compared to 4. 2 μm by 20 kV EPMA, whereas interfaces within pyroxene can be as narrow as 400 nm. Furthermore there are insufficient EPMA analyses to accurately describe the chemical profile across this interface. The geometry of the initial profile can be further refined by taking the measured profile of a slow diffusing element such as along the NaSi-CaAl exchange vector in plagioclase (Grove et al., 1984; Morse, 1984) or Ti in pyroxene (Cherniak & Liang, 2012), assuming diffusion has not modified these profiles extensively and using these profiles as the initial condition. However, this does depend on having a method that can analyse all the elements of interest at comparable length scale. With FEG-EPMA this would mean all elements of interest would need to be analysed at the same accelerating voltage, which is currently problematic in some cases, not least as emitted X-rays will emerge from different volumes dependent on their energy.

The generic Fe-Mg profile of a boundary between core and rim of an orthopyroxene crystal in Figure 11b, is modelled at the same conditions as described above. The starting condition is the assumed step-function profile and results in a timescale of 1.12 years. Assuming that with further refinement of the analytical protocol, Ti could

be analysed at the same resolution by FEG-EPMA and had a slightly inclined profile (red initial condition, Figure 11b) the calculated timescale is 1.07 years, an error of 18 days, which is less than the average error of ± 6 months due to a 20 °C uncertainty in magmatic temperature. Thus taking a step-function as the initial condition is a reasonable assumption, in simple 1D diffusion models, where the crystal zoning is suitable (e.g. pyroxenes in this study). However this assumption may need to be carefully considered when investigating short timescales or interfaces where step-profiles are not applicable.

Figure 11

4.2 Comparison of techniques

Each of the techniques discussed has their advantages and disadvantages (Table 3). FEG-EPMA analyses have the major advantage of quantitation at a nanoscale spot size. These analyses are time-consuming; for example, a 10 μm profile with 300 nm spacing takes over 7 hours to complete and may need to be repeated several times to gain the chemical composition of both majors and traces at optimal conditions. The inability to simultaneously measure all elements in one analysis introduces extra complexities, as adjacent profiles are required which can cause mismatches in profiles if they are not exactly parallel to each other and can necessitate the aligning of profiles at different spatial resolutions, causing additional complications. FEG-EPMA analyses for geologic applications at 5 kV at the nanoscale spatial resolution are at the early stages of protocol development. Issues have arisen due to carbon contamination (e.g. Buse and Kearns, 2013) and beam damage both of which are exacerbated at

these conditions resulting in the loss of intensity of elements after only a few seconds. Under these conditions when analysing with a low over-voltage the x-ray yield of some elements will restrict the detectability of the minor and trace elements, e.g. K in plagioclase. Whilst these issues can complicate analyses, comparison of profiles with high 20 kV EPMA signifies that high precision and accurate analyses can be achieved. In comparison both NanoSIMS and TOF-SIMS are generally qualitative rather than quantitative, although some recent studies have attempted quantification with matrix-matched standards (e.g. Maquis et al., 2010). However, both NanoSIMS and TOF-SIMS have the advantage of being able to analyse light elements such as Li, whereas EPMA techniques are currently limited to elements with atomic number 5 and above.

5. Conclusions

NanoSIMS, TOF-SIMS and FEG-EPMA can all achieve chemical profiles of zoned crystals at the nanoscale for a range of elements. NanoSIMS and TOF-SIMS permit relative concentrations of a large range of elements to be attained. Diffusion chronometry that relies on concentration gradients can therefore exploit chemical profiles, widening the potential number of elements that can be modelled and timescales calculated. FEG-EPMA in addition permits quantitative analyses of plagioclase and pyroxene at the same resolution that can also be employed in diffusion chronometry studies, for crystal forensic studies which investigate the genesis of the crystals and thus the magmatic plumbing system.

The increased spatial resolution of these techniques has demonstrated sharp (<2μm) internal compositional boundaries within zoned minerals that have not been

extensively modified through diffusional processes. Thus, assuming a step-function profile in simple 1D diffusion models, for suitable crystals such as pyroxene is realistic, as calculated errors are smaller than those introduced from magmatic temperature uncertainties. This could be refined using measured profiles of slow diffusion elements such as NaSi-CaAl and Ti in plagioclase and orthopyroxene respectively as the initial condition.

The ability to analyse materials at a nanoscale in the geological sciences is growing. Diffusion chronometry is only one potential application; other examples include the analysis of small experimental charges, the investigation of mineral boundaries, melt inclusions, the zonation of corals and foraminifera or mineral nodules. The analytical protocols described here are transferable, the most suitable method being dependant on the aim of the study and the elements of interest.

Acknowledgements

This work was supported by a National Environment Research Council post-doctoral fellowship (NE/G0129X/1) to KS and ERC Advanced Grant (CRITMAG) to JB. The authors acknowledge the facilities, scientific and technical assistance of the Australian Microscopy and Microanalysis Research Facility at the Centre for Microscopy, Characterisation and Analysis, the University of Western Australia, a facility funded by the University, State and Commonwealth Governments.

Figure Captions

Figure 1. Monte Carlo simulation for labradorite plagioclase at 15 kV and 5kV accelerating voltage. Electron interaction volume is shown (with red lines displaying

backscattered electrons). Contours give modelled beam electrons energy showing the energy loss away from point of beam impact.

Figure 2. (a) BSE images summarising the texture of the four analysed plagioclase crystals, with locations of analyses marked. The additional line of grey dots on the June crystal are previous craters (round holes) from SIMS analysis by Berlo et al. (2004). (b) ^{39}K NanoSIMS images at two magnifications and a comparison BSE image of August plagioclase crystal. ^{39}K highlights the anorthite banding and melt inclusions observed in BSE image; the NanoSIMS profile; previous NanoSIMS analysis (square crater); and the high kV EPMA profile. (c) BSE images summarising the textural of the orthopyroxene crystals previously analysed by EPMA and TOF-SIMS (Saunders et al., 2012b) and further analysed by low kV FEG-EPMA. Locations of EPMA and low kV FEG-EPMA analysis are shown.

Figure 3. ZAF corrected profiles of MgO, FeO and SrO profiles ofJuly 22, MSH plagioclase crystal using the major element composition of the two extreme compositions (An_{37} and An_{64}) observed within the major element profile. Calculated MgO, FeO and SrO concentrations are almost identical. Therefore only a single major element composition is required for use with the ZAF correction. Minimum detection limits for the operating conditions used are 72ppm, 20ppm, 275ppm for Sr, Mg, Fe respectively.

Figure 4. Comparison of FEG-EPMA analyses of orthopyroxene crystals for differing spatial resolution. Profiles for Mg (a) and Al (b) are shown for crystal A using the specified setup. Note crystal rim is located at 0 micrometres.

Figure 5. Comparison of major element spot analyses (800 nm spot spacing) to line scans both by low kV FEG-EPMA of a plagioclase crystal. Error bars on the x-axis represent the excitation area of analyses and the 2SD analytical uncertainty on the y-axis. Note the difference in trend between 16 μm – 22 μm is due to the slight difference in line orientation and variation in crystal zonation that is observed within the crystal. Errors represent the excitation volume on the x-axis and the propagation of the 2SD analytical uncertainty on the y-axis.

Figure 6. Sub-micrometre major element profiles of MSH orthopyroxene. (a) Comparison of low kV FEG-EPMA and TOF-SIMS analyses. (b) Low kV FEG-EPMA spot and line analyses of orthopyroxene. Note the mismatch between lines is due to a combination of the two profiles not being perpendicular to one another and changes in the crystal chemistry along the interface.

Figure 7. Comparison of cumulative ^{44}Ca counts to $^{44}Ca/^{28}Si$ counts of the medium May line scan.

Figure 8. NanoSIMS element profiles of May plagioclase crystal at range of scales; (a) coarse line scan (b) medium line scan (c) the fine line scan (d) finest-scale line scan. For each profile the high kV EPMA profile is shown as a comparison, with the wt. % compositions converted to X/Si. High kV EPMA errors represent the excitation volume on the x-axis and the propagation of the 2SD analytical uncertainty on the y-axis. NanoSIMS errors represent the beam diameter on the x-axis and counting errors on the y-axis.

Figure 9. Sr correlation of low kV FEG-EPMA and SIMS techniques. SIMS minimum detection limit 0.3ppm

Figure 10. Comparison of high kV EPMA, low kV FEG-EPMA spot and low kV FEG-EPMA line analyses for diffusion chronometry studies of a MSH orthopyroxene crystal. High kV EPMA ellipses show the calculated excitation volume on the x-axis and the 2.s.d. analytical errors on the y-axis. High kV EMPA and low kV FEG-EPMA spot analyses cannot be modelled due to insufficient data points across the profile. High kV EPMA data is from Saunders et al. (2012b). Calculated timescale for the low kV FEG-EPMA line analysis is calculated assuming the Fe counts represent the same Fe-Mg profile as extracted from and modelled using the same parameters (880 °C, $D_{Fe-Mg} = 3.19 \times 10^{-20}$ m^2/s) as for the BSE image (see text for further details). Note the line analysis was performed across the boundary only and not to the crystal rim. Error bars for low kV FEG-EPMA are the calculated excitation volume on the x-axis and 2 SD analytical errors on the y-axis for spot analyses and the square root of counts for the line analyses.

Figure 11. (a) Increase spatial resolution of Ca profiles across the core-rim interface of the 18th May MSH plagioclase crystal. Detail NanoSIMS profile reveals the core-rim interface is much sharper than the low kV FEG-EPMA and high kV EPMA profiles, which are artificially broaden due to the limited spatial resolution of the analytical technique. (b) Demonstration in the difference in calculated timescales that may result from assuming an initial step function profile compared to an initial profile determined by a slow diffusing element such as NaSi-CaAl exchange in plagioclase or Ti in pyroxene. The model profile is a Fe-Mg profile of a core-rim orthopyroxene boundary; modelled using the D_{Fe-Mg} coefficients of Ganguly and Tazzoli (1994) at

880 °C. Calculated timescale is 1.12 years with an initial step function profile (black), compared to a timescale of 1.07 years with an initially inclined boundary (red).

Table Captions

Table 1. Reference materials characterised at high voltage (20kV) and low (5kV) voltage using methods described.

Table 2. Minimum characteristic timescales that can be calculated for diffusion modelling at a spatial resolution of 2 μm for high kV EPMA and 500 nm for low kV FEG-EPMA for plagioclase crystals for a range of elements.

Table 3. Comparison of high kV EPMA, low kV FEG-EPMA, NanoSIMS and TOF-SIMS, highlighting the advantages and disadvantage of each technique that are relevant to this study. Please see text for full details of each method.

Supplementary Data

Supplementary data: EPMA, FEG-EPMA & NanoSIMS data of plagioclase crystals and FEG-EPMA of orthopyroxene crystals.

Supplementary Figure 1: Characterisation of June plagioclase EPMA profiles to coarse, medium and fine NanoSIMS data to line scans. EPMA profiles to coarse, medium, fine and detail NanoSIMS data to line scans. Note for direct comparison EPMA profiles have been converted to X/Si in wt.%. EPMA errors represent the excitation volume on the x-axis and the propagation of the 2SD analytical uncertainty on the y-axis. NanoSIMS errors represent the beam diameter on the x-axis and counting errors on the y-axis. SIMS errors represent the spot size on the x-axis and the reported analytical uncertainty of Berlo et al. (2007) on the y-axis.

Supplementary Figure 2: Characterisation of July plagioclase EPMA profiles to medium, fine and detail NanoSIMS data to line scans. EPMA profiles to coarse, medium, fine and detail NanoSIMS data to line scans. Note for direct comparison EPMA profiles have been converted to X/Si in wt.%. EPMA errors represent the excitation volume on the x-axis and the propagation of the 2SD analytical uncertainty on the y-axis. NanoSIMS errors represent the beam diameter on the x-axis and counting errors on the y-axis. Note K was not analysed for the coarse NanoSIMS profile.

Supplementary Figure 3: Characterisation of August plagioclase EPMA profiles to coarse, medium and fine NanoSIMS data to line scans. EPMA profiles to coarse, medium, fine and detail NanoSIMS data to line scans. Note for direct comparison EPMA profiles have been converted to X/Si in wt.%. EPMA errors represent the excitation volume on the x-axis and the propagation of the 2SD analytical uncertainty on the y-axis. NanoSIMS errors represent the beam diameter on the x-axis and counting errors on the y-axis. Note no coarse profile is available as it failed mid-analysis.

References

Abramoff, M.D., Magalhaes, P.J., Ram, S.J. 2004. Image processing with ImageJ. Biophotonics International, 11, 36-42.

Armstrong, J.T., Crispin, K.L. 2012. Current Limitations in the Use of L-Lines of First-Row Transition Elements for Quantitative EDS and WDS Analysis of Complex Materials. Microscopy and Microanalysis, 18 (Suppl 2), 1726-1727

Berlo, K., Blundy, J., Turner, S., Cashman, K., Hawkesworth, C., Black, S. 2004. Geochemical precursors to volcanic activity at Mount St. Helens, USA. Science 306, 1167-1169.

Berlo, K., Blundy, J., Turner, S., Hawkesworth, C. 2007. Textural and chemcial variation in plagioclase phenocrysts from the 1980 eruptions of Mount St. Helens, USA. Contributions to Mineralogy and Petrology 154, 291-308.

Buse, B., Kearns, S. 2013. Carbon contamination in silicate minerals during low voltage FE-EPMA: when is it important? EMAS 13th European Workshop on Modern Developments and Applications in Microbeam Analysis.

Charlier, B.L.A., Wilson, C.J.N., Lowenstern, J.B., Blake, S., Van Calsteren, P.W., Davidson, J.P., 2005. Magma generation at a large, hyperactive silicic volcano (Taupo, New Zealand) revealed by U-Th and U-Pb systematics in zircons. Journal of Petrology 46, 1875-1894.

Charlier, B.L.A., Wilson, C.J.N., Davidson, J.P., 2008. Rapid open-system assembly of a large silicic magma body: time-resolved from cored plagioclase crystals in the Oruanui eruption deposits, New Zealand. Contributions to Mineralogy and Petrology 156, 799-813.

Charlier, B.L.A., Morgan, D.J., Wilson, C.J.N., Wooden, J.L., Allan, A.S.R., Baker, J.A., 2012. Lithium concentration gradients in feldspar and quartz record the final minutes of magma ascent in an explosive supereruption. Earth and Planetary Science Letters 319-320, 218-227.

Cherniak, d.J., 2002. Ba diffusion in feldspar. Geochimica et Cosmochimica Acta 66, 1641-1650.

Cherniak, D.J., Liang, Y., 2012. Ti diffusion in natural pyroxene. Geochimica et Cosmochimica Acta 98, 31-47.

Claiborne, L.L., Miller, C.F., Flanagan, D.M., Clynne, M.A., Wooden, J.L., 2010. Zircon reveals protracted magma storage and recycling beneath Mount. St. Helens. Geology 38, 1011-1014.

Costa, F. Morgan, D. 2010. Time constraints from chemical equilibrium in magmatic crystals. In Dosseto, A., Turner, S.P., & Van-Orman, J.A. (eds) Timescales of magmatic processes: From cores to atmosphere. Wiley-Blackwell, New York.

Costa, F., Chakraborty, S., Dohmen, R. 2003. Diffusion coupling between trace and major elements and a model for calculation of magma residence times using plagioclase. Geochimica et Cosmochimica Acta 67, 2189-2200.

Costa. F., Dohmen, R., Chakraborty, S., 2008. Time scales of magmatic processes from modelling the zoning patterns of crystals. Reviews in Mineralogy & Geochemistry 69, 545-594.

Druit, T.H., Costa, F., Deloule, E., Dungan, M., Scailet, B., 2012. Decadal to monthly timescales of magma transfer and reservoir growth at a caldera volcano. Nature 482, 77-80.

Ganguly, J., Tazzoli, V., 1994. Fe^{2+}-Mg interdiffusion in orthopyroxene: Retrieval from the data on intracrystalline exchange reaction. American Mineralogist 79, 930-937.

Genareau, K., Hervig, R., & Clarke, A. 2007. Geochemical variations in late-stage growth of volcanic phenocrysts revealed by SIMS depth-profiling. American Mineralogist 79, 930-937.

Giletti, B.J, Casserly, J.E.D., 1994. Strontium diffusion kinetics in plagioclase feldspars. Geochimica et Cosmochimica Acta 58, 3785-3793.

Giletti, B.J., Shanahan, T.M., 1997. Alkali diffusion in plagioclase feldspar. Chemical Geology, 139, 3-20.

Ginibre, C., Kronz, A., Wörner, G., 2002. High-resolution quantitative imaging of plagioclase composition using accumulated backscattered electron images: new constraints on oscillatory zoning. Contributions to Mineralogy and Petrology 142, 436-448.

Goldstein, J.I., Newbury, D.E., Echlin, P., Joy, D.C., Lyman, C.E., Lifshin, E., Sawyer, L., and Michael, J.R., 1992, Scanning Electron Microscopy and X-ray Microanalysis, 2nd ed., Kluwer Academic / Plenum Publishers, New York.

Grove, T.L., Baker, M.B., Kinzler, R.J. 1984. Coupled CaAl-NaSi diffusion in plagioclase feldspar: Experiments and applications to cooling rate speedometry. Geochimica et Cosmochimica Acta 48, 2113-2121.

Humphreys, M.C.S., Menand, T., Blundy, J.D., Klimm, K., 2008. Magma ascent rates in explosive eruptions: Constraints from H_2O diffusion in melt inclusions. Earth and Planetary Science Letters 270, 25-40.

Jarosewich, E., Nelen, J.A., Norberg, J.A., 1980. Reference samples for electron microprobe analysis. Geostandards Newsletter 4, 43-47.

Kahl, M., Chakraborty, S., Costa, C., Pompilio, M., 2011. Dynamic plumbing system beneath volcanoes revealed by kinetic modelling, and the connection to monitoring data: An example from Mt. Etna. Earth and Planetary Science Letters 308, 11-22.

Kent, A.J.R., Blundy, J., Cashman, K.V., Cooper, K.M., Donnelly, C., Pallister, J.S., Reagan, M., Rowe, M.C., & Thornber, C.R. 2007. Vapor transfer prior to the October 2004 eruption of Mount St. Helens, Washington. Geology 35, 231-234.

LaTourrette, T., Wasserburg, G.J. 1998. Mg diffusion in anorthite: Implications for the formation of early solar system planetesimals. Earth and Planetary Science Letters 158, 91-108.

Martin, V.M., Morgan, D.J., Jerram, D.A., Caddick, M.J., Prior, D.J., Davidson, J.P. 2007. Bang! Month-scale eruption triggering at Santorini volcano. Science 321, 1178.

Marques, A.F.A., Scott, S.D., Sodhi, R.N.S., 2010. Determining major and trace element compositions of exposed melt inclusions in minerals using TOF-SIMS. Surface and International Analysis 43, 436-442.

Merlet, C., and Llovet, X. 2012 Uncertainty and capability of quantitative EPMA at low voltage – A review. IOP Conf. Ser.: Mater. Sci. Eng. **32** 012016

McPhail, D.S., 2006. Applications of Secondary Ion Mass Spectrometry (SIMS) in Materials Science. Journal of Material Science 41, 873-903.

McSwiggen P., 2013 Characterization of sub-micrometer features with the FE-EPMA. EMAS 13th European Workshop on Modern Developments and Applications in Microbeam Analysis.

Morgan, D.J., Blake, S., Rogers, N.W., DeVivo, B., Rolandi, G., Macdonald, R & Hawkesworth, C.J. (2004). Time scales of crystal residence and magma chamber volume from modelling of diffusion profiles in phenocrysts: Vesuvius 1944. Earth and Planetary Science Letters 222, 933-946.

Morse, S.A.,1984. Cation diffusion in plagioclase feldspar. Science 225, 504-505.

Reed, S.J.B., 1996. Electron Microprobe Analysis, 2nd edition. Cambridge University Press, UK.

Rowe, M.C., Kent, A.J.R., Thornber, C.R., 2008. Using amphibole phenocrysts to track vapour transfer during magma crystallization and transport: An example from Mount St. Helens, Washington. Journal of Volcanology and Geothermal Research 178, 593-607.

Saunders, K.E., Morgan, D.J., Baker, J.A., Wysoczanski, R.J. 2010. The magmatic evolution of the Whakamaru supereruption, New Zealand constrained by microanalytical study of plagioclase and quartz. Journal of Petrology, 51, 2465-2488.

Saunders, K.E., Blundy, J., Dohmen, R., Cashman, K. 2012a. Linking petrology and seismology at an active volcano. Science 336, 1023-1027.

Saunders, K., Rinnen, S., Blundy, J., Dohmen, R., Klemme, S., Arlinghaus, H.F., 2012b. TOF-SIMS and electron microprobe investigation of zoned magmatic orthopyroxenes: First results of trace and minor element analysis with implications for diffusion modelling. American Mineralogist 97, 532-542.

Wark, D.A., Hildreth, W., Spear, F.S., Cherniak, D.J., Watson, E.B. 2007. Pre-eruption recharge of the Bishop magma system. Geology 35, 235-238.

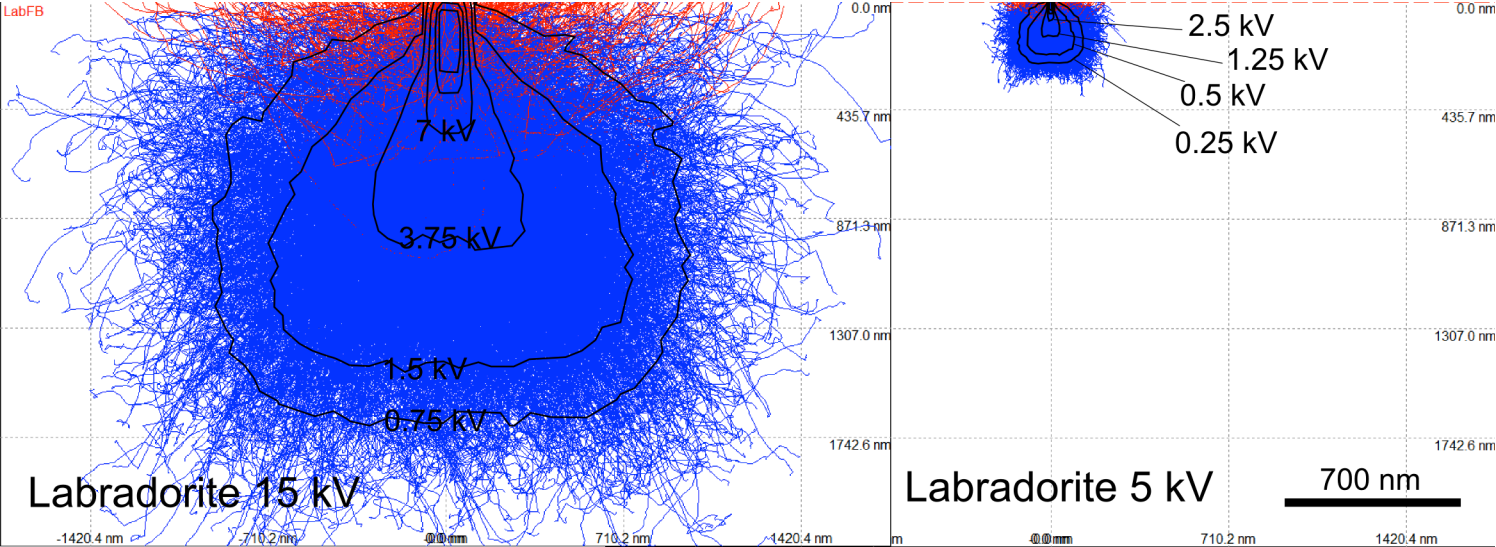
LabFB
7 kV
3.75 kV
1.5 kV
0.75 kV
0.0 nm
435.7 nm
871.3 nm
1307.0 nm
1742.6 nm
Labradorite 15 kV
-1420.4 nm
-710.2 nm
710.2 nm
1420.4 nm
2.5 kV
1.25 kV
0.5 kV
0.25 kV
Labradorite 5 kV
700 nm

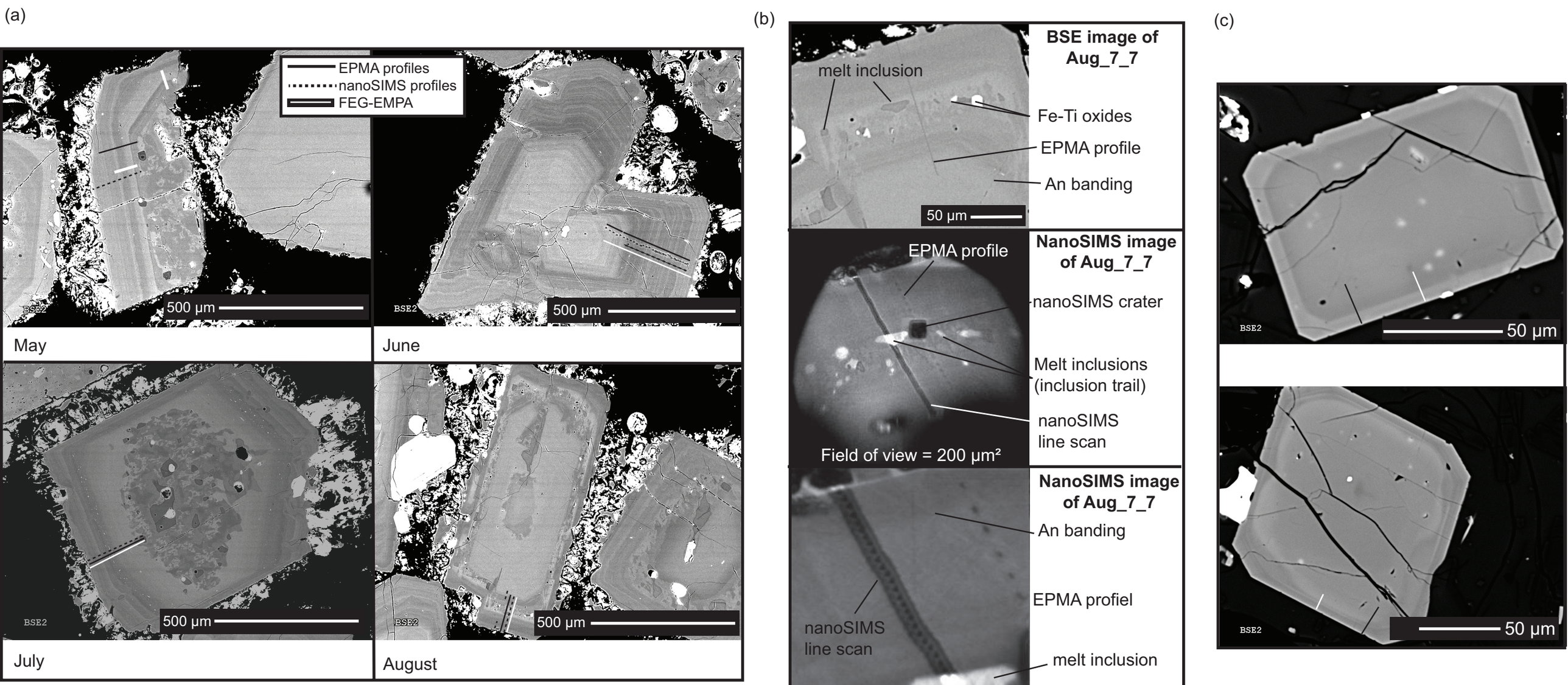
(a)
EPMA profiles
nanoSIMS profiles
FEG-EMPA
500 µm
BSE2
May
June
July
August
(b)
BSE image of Aug_7_7
melt inclusion
Fe-Ti oxides
EPMA profile
An banding
50 µm
NanoSIMS image of Aug_7_7
EPMA profile
nanoSIMS crater
Melt inclusions (inclusion trail)
nanoSIMS line scan
Field of view = 200 µm²
NanoSIMS image of Aug_7_7
An banding
EPMA profiel
nanoSIMS line scan
melt inclusion
Field of view = 60 µm²
(c)
50 µm

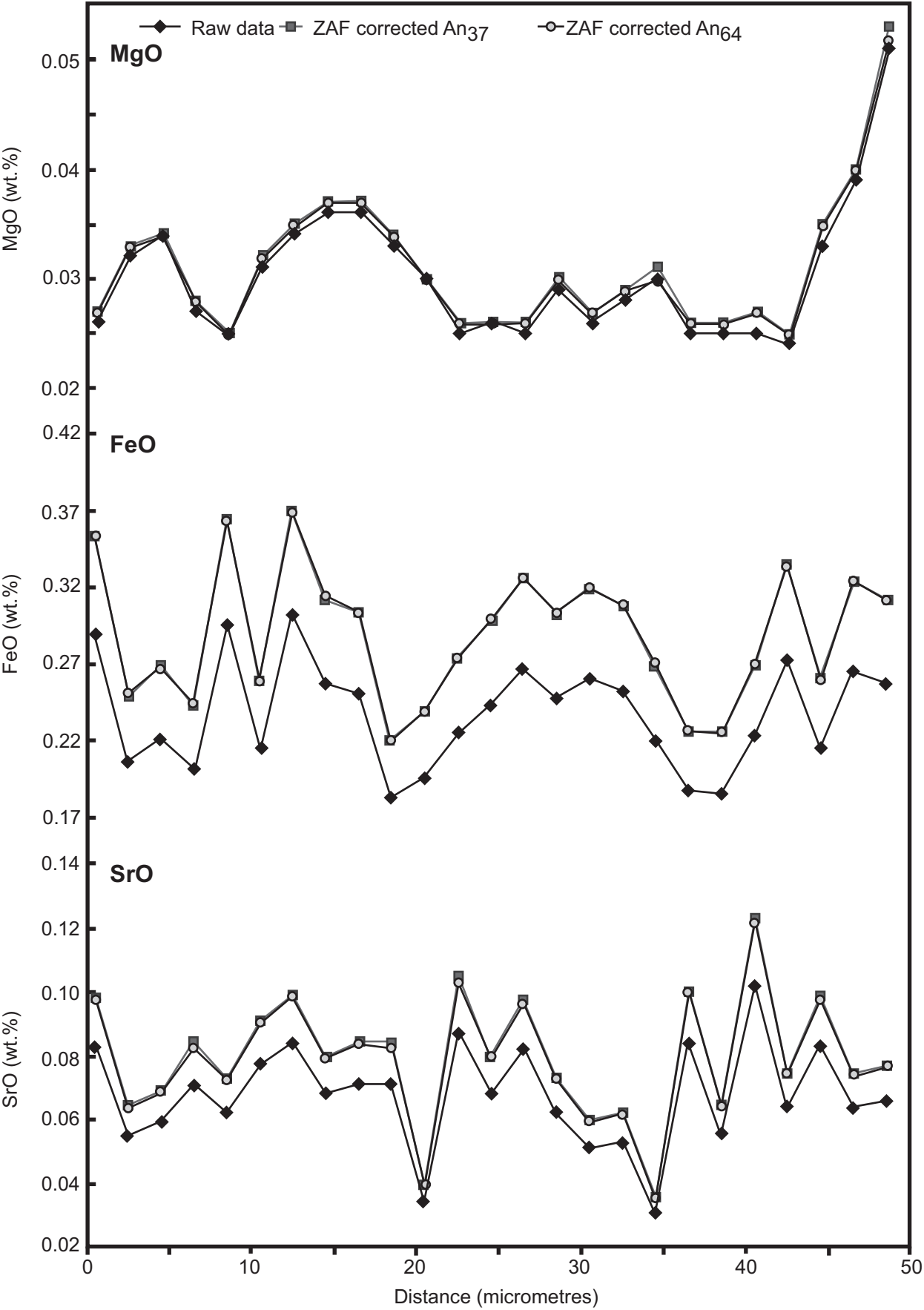
Raw data
ZAF corrected An37
ZAF corrected An64
MgO
FeO
SrO
MgO (wt.%)
FeO (wt.%)
SrO (wt.%)
0.05
0.04
0.03
0.02
0.42
0.37
0.32
0.27
0.22
0.17
0.14
0.12
0.10
0.08
0.06
0.04
0.02
0
10
20
30
40
50
Distance (micrometres)

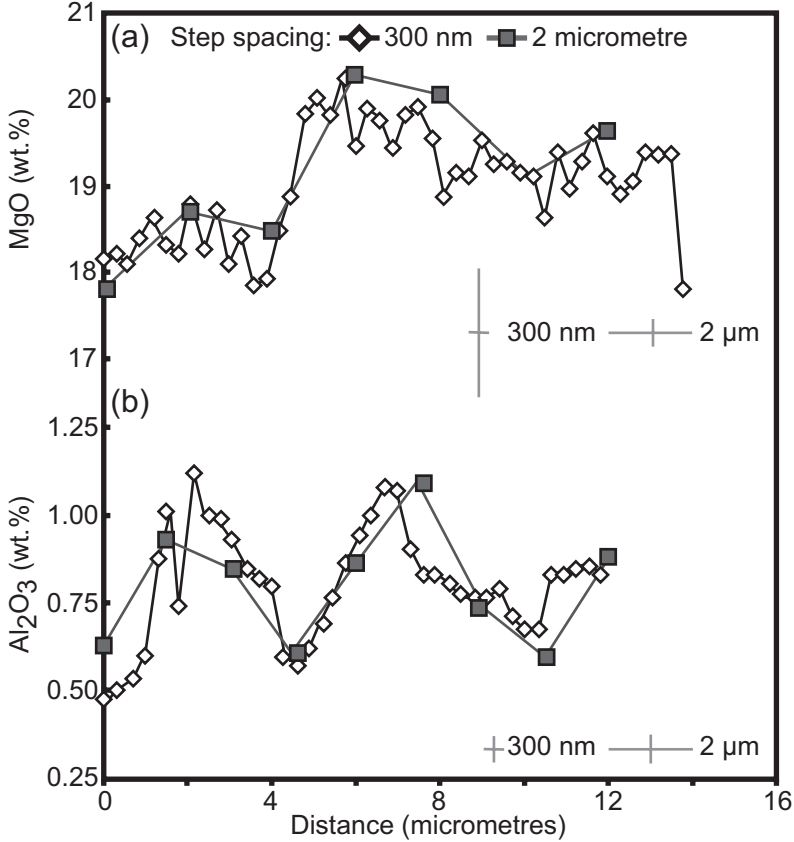
(a)
Step spacing:
300 nm
2 micrometre
MgO (wt.%)
21
20
19
18
17
300 nm
2 µm
(b)
Al2O3 (wt.%)
1.25
1.00
0.75
0.50
0.25
300 nm
2 µm
0
4
8
12
16
Distance (micrometres)

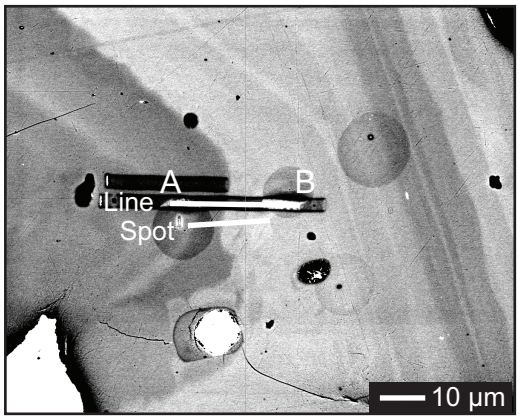
A
B
Line
Spot
10 µm

Line Spot

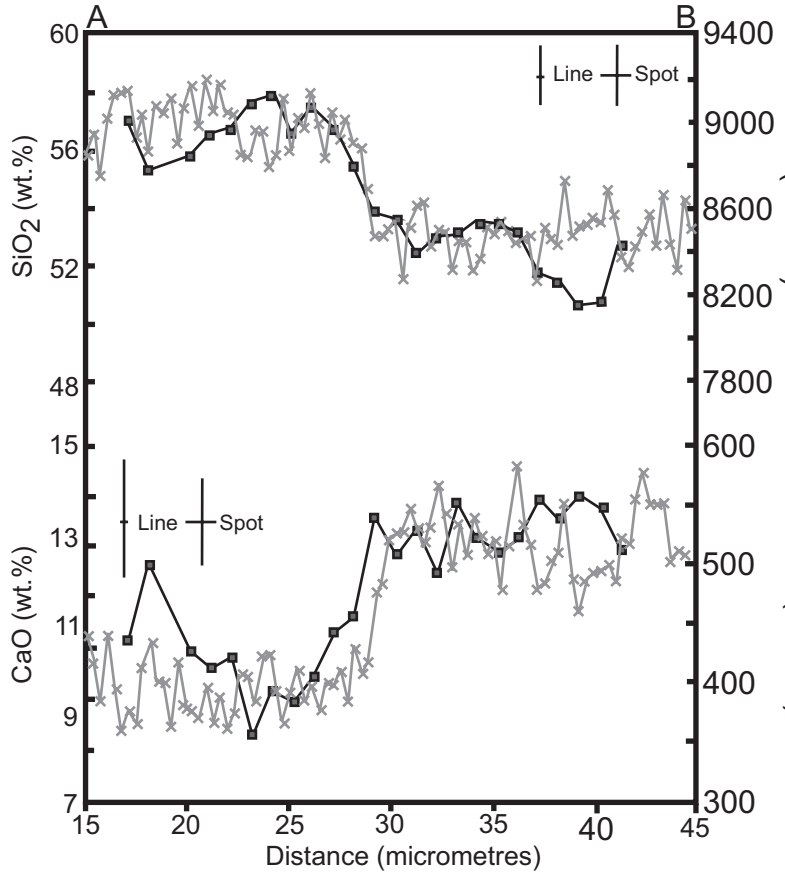
A
B
Line
Spot
SiO2 (wt.%)
Si (counts)
CaO (wt.%)
Ca (counts)
Distance (micrometres)

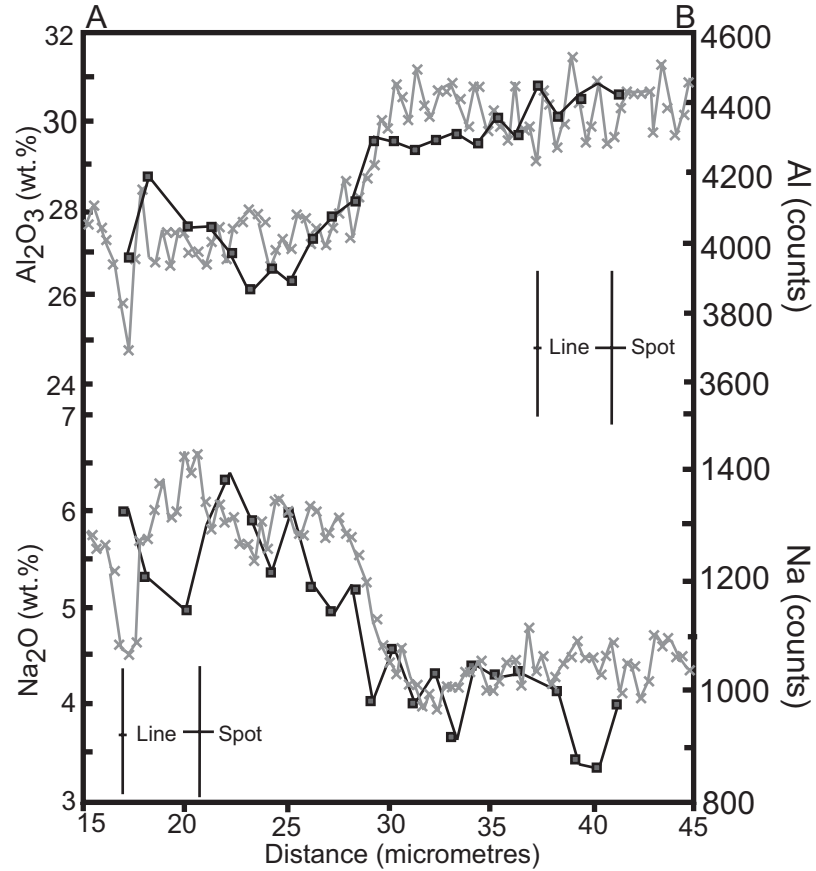
A
B
Line
Spot
Al2O3 (wt.%)
Al (counts)
Na2O (wt.%)
Na (counts)
Distance (micrometres)

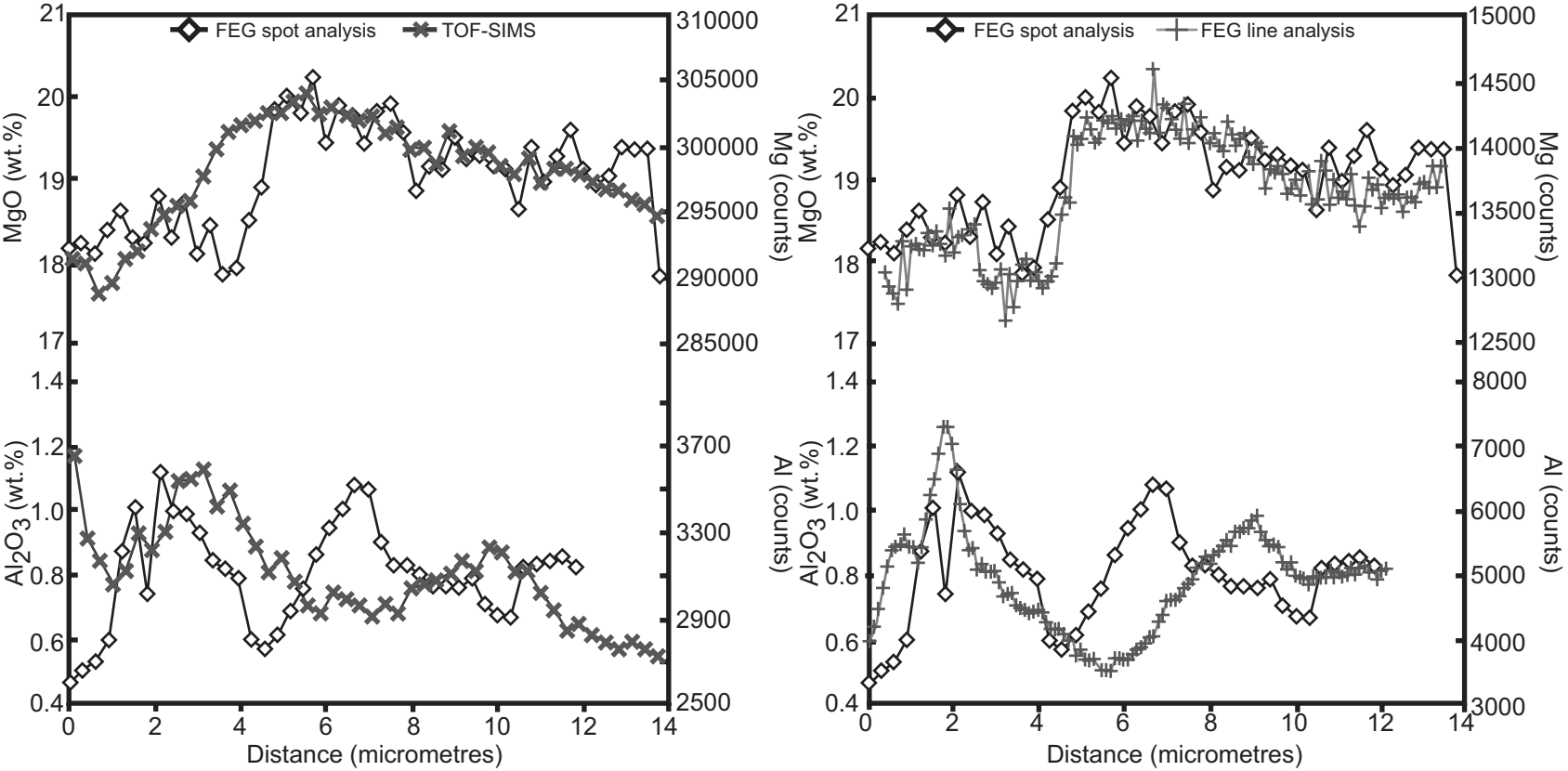
FEG spot analysis
TOF-SIMS
MgO (wt.%)
Mg (counts)
Al2O3 (wt.%)
Al (counts)
Distance (micrometres)
FEG spot analysis
FEG line analysis
MgO (wt.%)
Mg (counts)
Al2O3 (wt.%)
Al (counts)
Distance (micrometres)

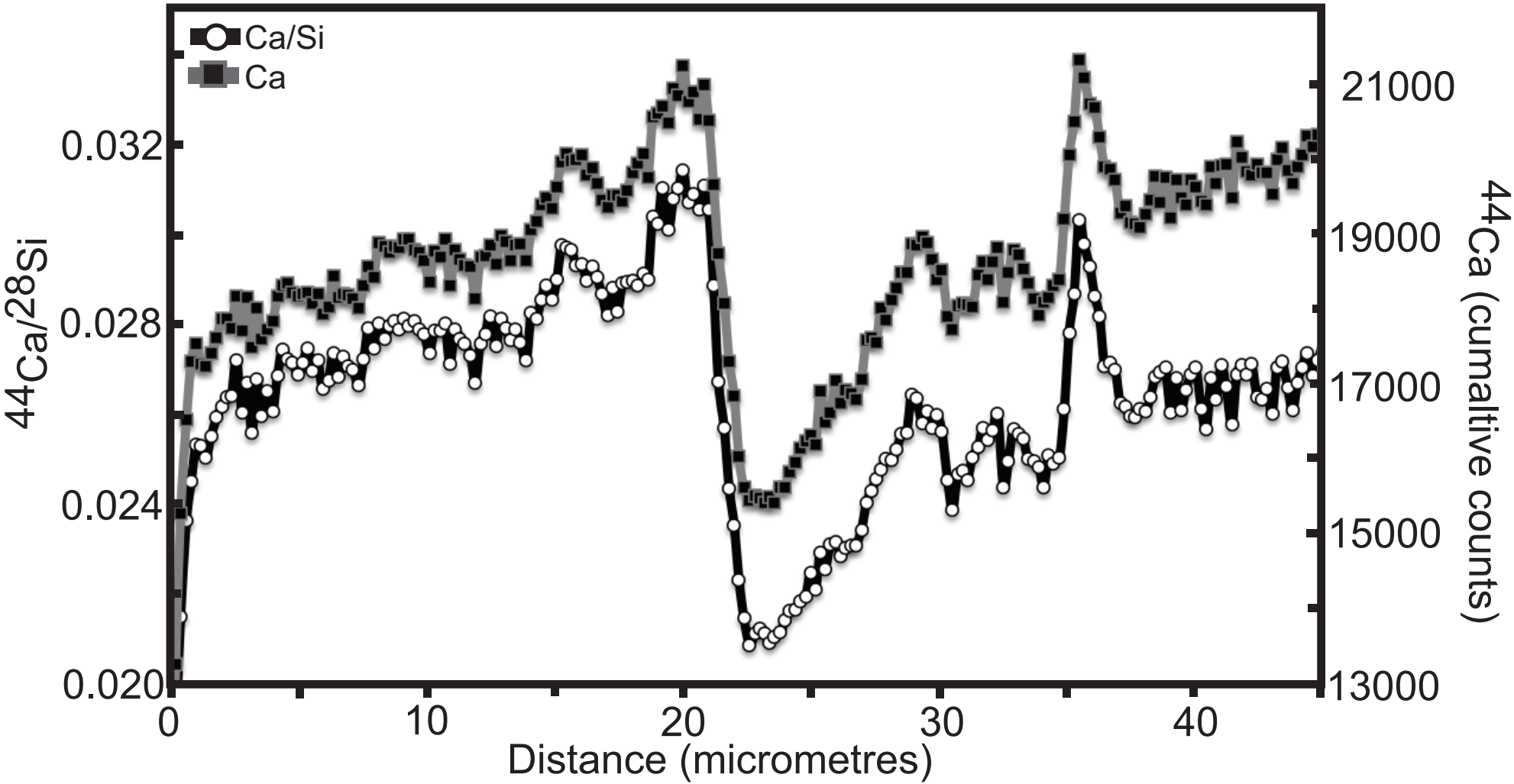
Ca/Si
Ca
0.032
0.028
0.024
0.020
$^{44}Ca/^{28}Si$
21000
19000
17000
15000
13000
^{44}Ca (cumaltive counts)
0
10
20
30
40
Distance (micrometres)

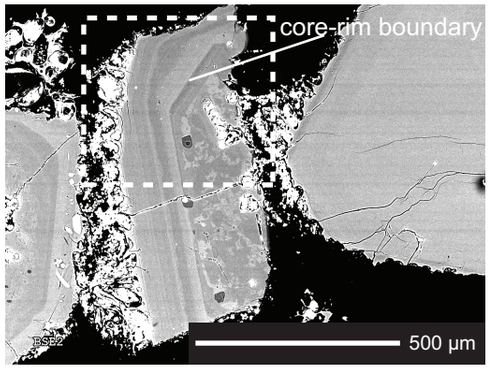
core-rim boundary
500 µm

May_18_1

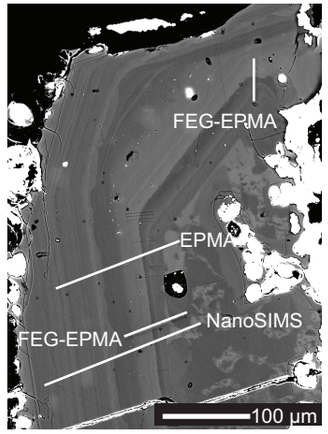
FEG-EPMA
EPMA
NanoSIMS
FEG-EPMA
100 µm

D

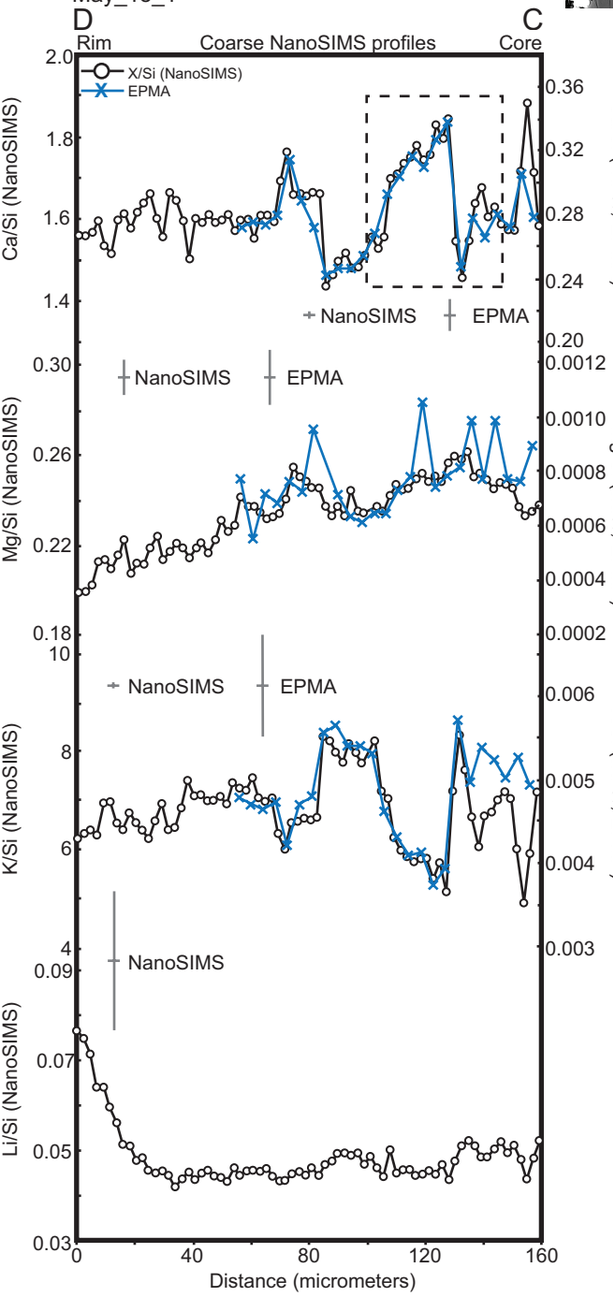
Rim
Coarse NanoSIMS profiles
Core
X/Si (NanoSIMS)
EPMA
NanoSIMS
EPMA
NanoSIMS
EPMA
NanoSIMS
Ca/Si (NanoSIMS)
Ca/Si (wt. %, EPMA)
Mg/Si (NanoSIMS)
Mg/Si (wt.%, EPMA)
K/Si (NanoSIMS)
K/Si (wt. %, EPMA)
Li/Si (NanoSIMS)
Distance (micrometers)

C

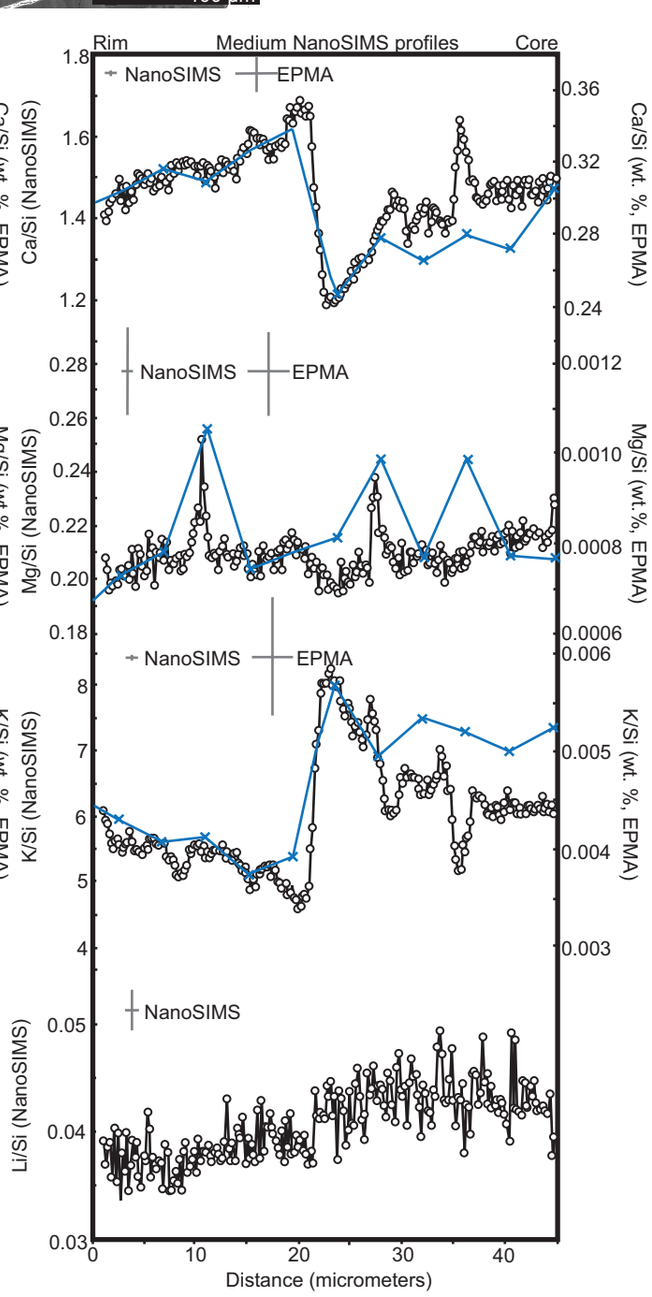
Rim
Medium NanoSIMS profiles
Core
NanoSIMS
EPMA
NanoSIMS
EPMA
NanoSIMS
EPMA
NanoSIMS
Ca/Si (NanoSIMS)
Ca/Si (wt. %, EPMA)
Mg/Si (NanoSIMS)
Mg/Si (wt.%, EPMA)
K/Si (NanoSIMS)
K/Si (wt. %, EPMA)
Li/Si (NanoSIMS)
Distance (micrometers)

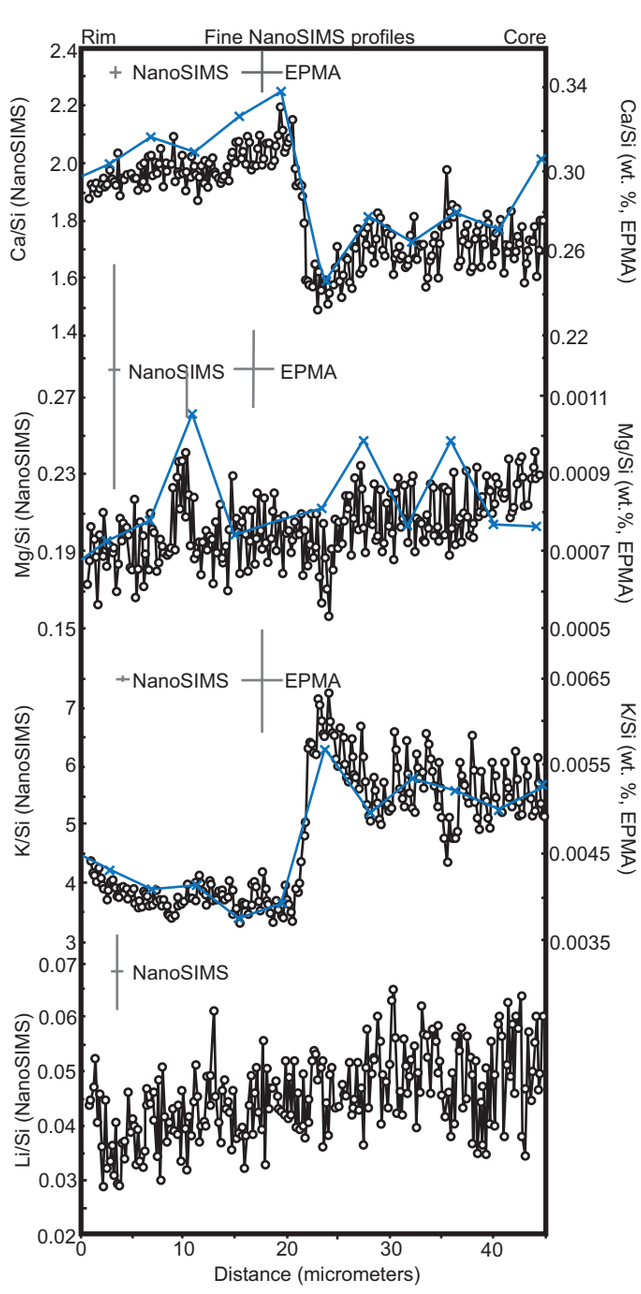
Rim
Fine NanoSIMS profiles
Core
NanoSIMS
EPMA
NanoSIMS
EPMA
NanoSIMS
EPMA
NanoSIMS
Ca/Si (NanoSIMS)
Ca/Si (wt. %, EPMA)
Mg/Si (NanoSIMS)
Mg/Si (wt.%, EPMA)
K/Si (NanoSIMS)
K/Si (wt. %, EPMA)
Li/Si (NanoSIMS)
Distance (micrometers)

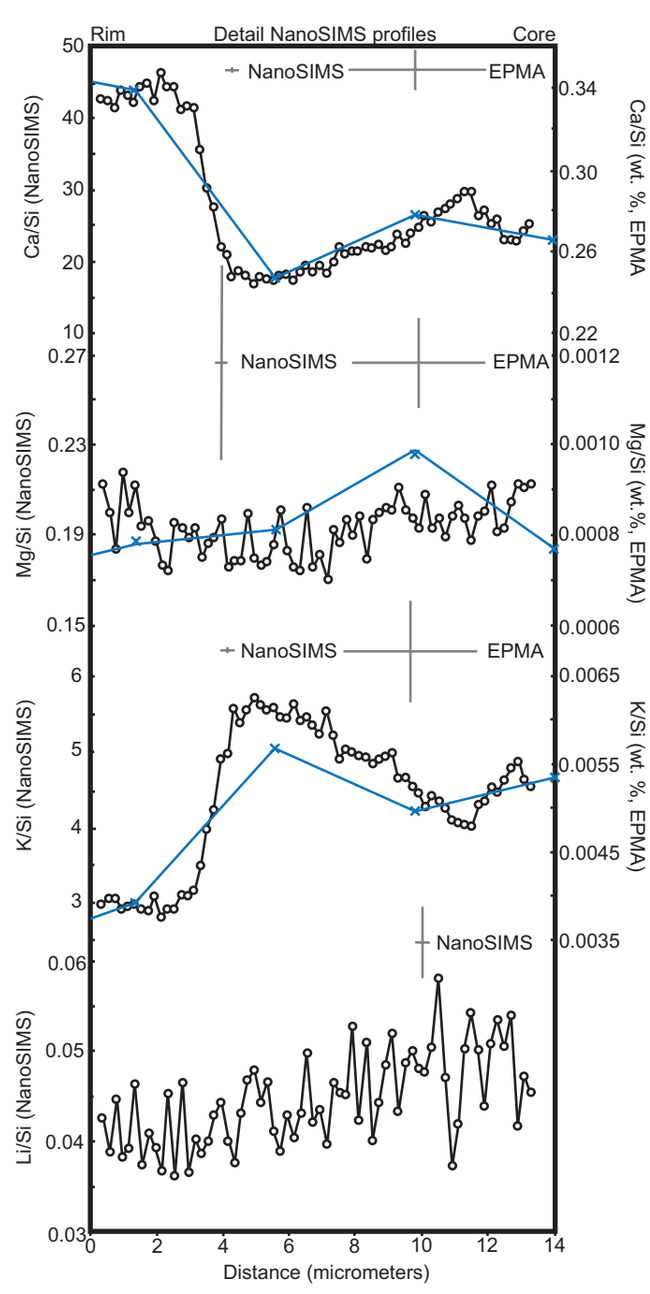
Rim
Detail NanoSIMS profiles
Core
NanoSIMS
EPMA
NanoSIMS
EPMA
NanoSIMS
EPMA
NanoSIMS
Ca/Si (NanoSIMS)
Ca/Si (wt. %, EPMA)
Mg/Si (NanoSIMS)
Mg/Si (wt.%, EPMA)
K/Si (NanoSIMS)
K/Si (wt. %, EPMA)
Li/Si (NanoSIMS)
Distance (micrometers)

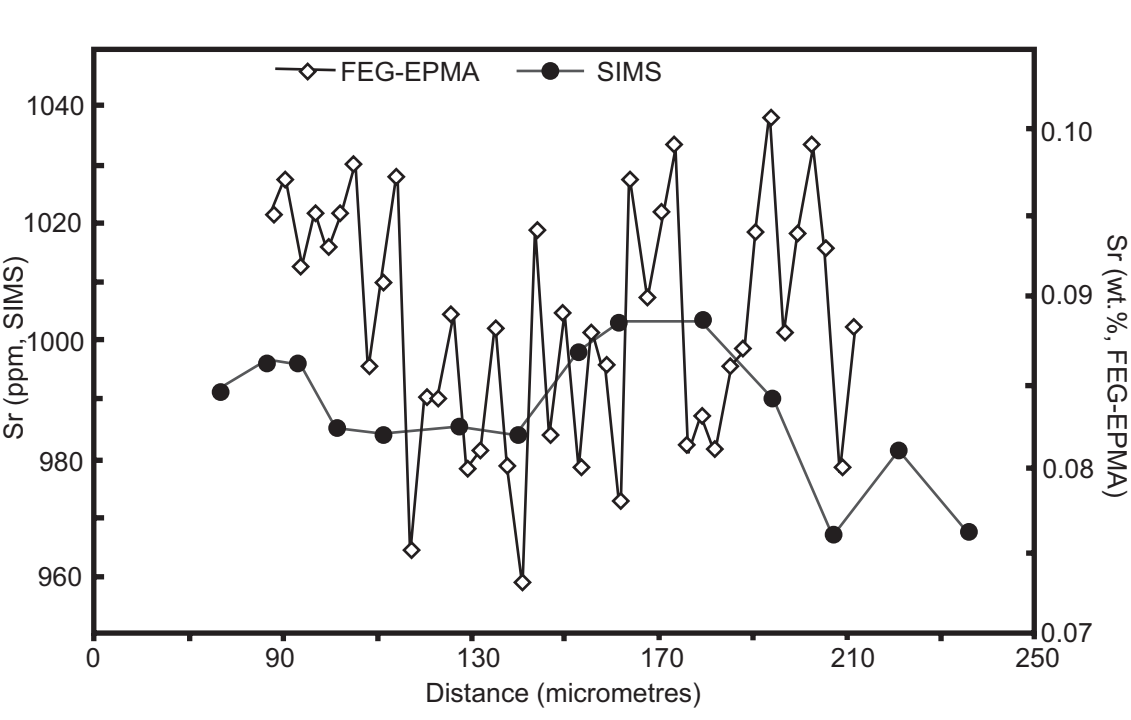
FEG-EPMA
SIMS
1040
1020
1000
980
960
Sr (ppm, SIMS)
0.10
0.09
0.08
0.07
Sr (wt.%, FEG-EPMA)
0
90
130
170
210
250
Distance (micrometres)

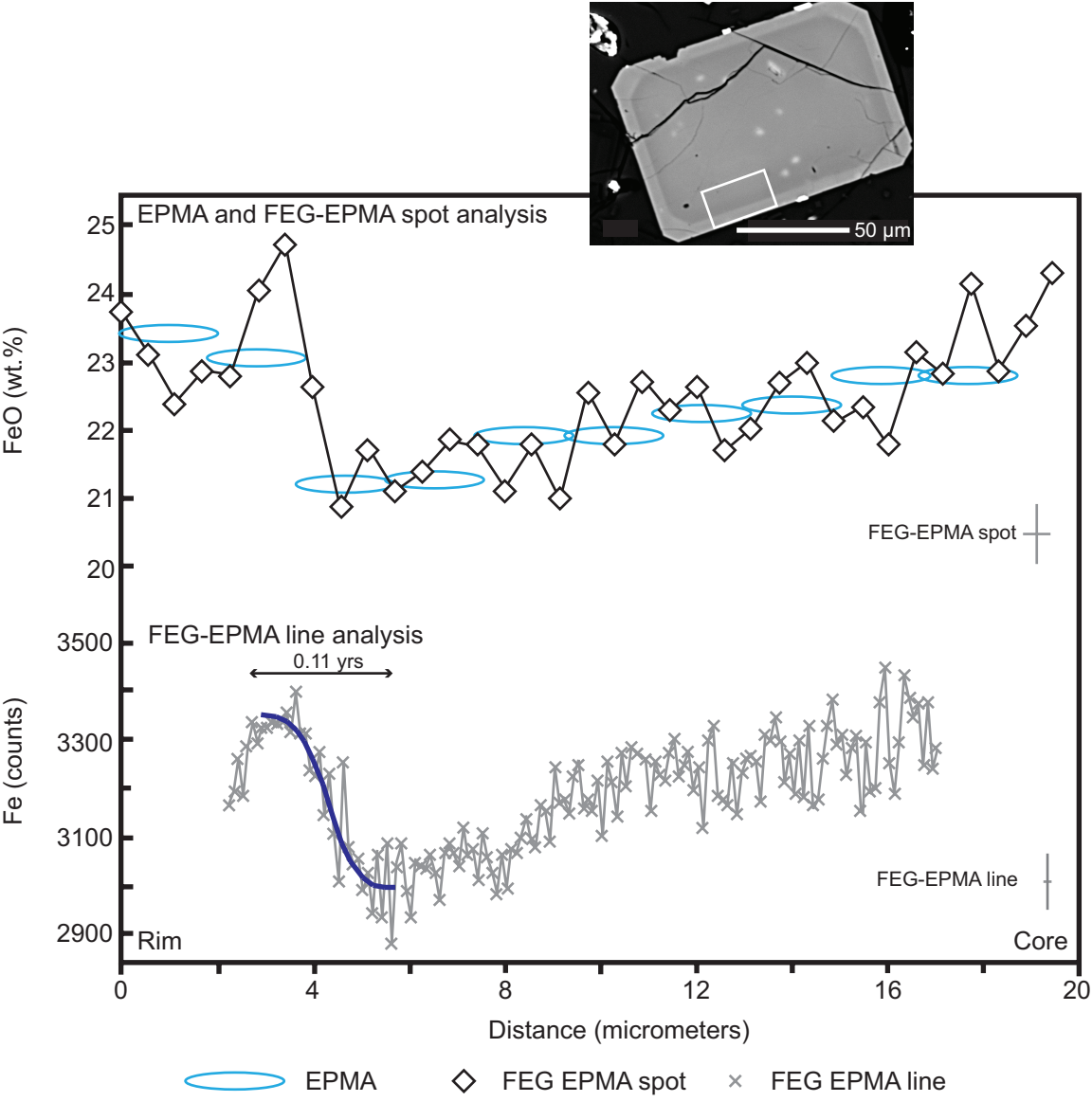
EPMA and FEG-EPMA spot analysis
50 µm
FeO (wt.%)
25
24
23
22
21
20
FEG-EPMA spot
FEG-EPMA line analysis
0.11 yrs
Fe (counts)
3500
3300
3100
2900
FEG-EPMA line
Rim
Core
0
4
8
12
16
20
Distance (micrometers)
EPMA
FEG EPMA spot
FEG EPMA line

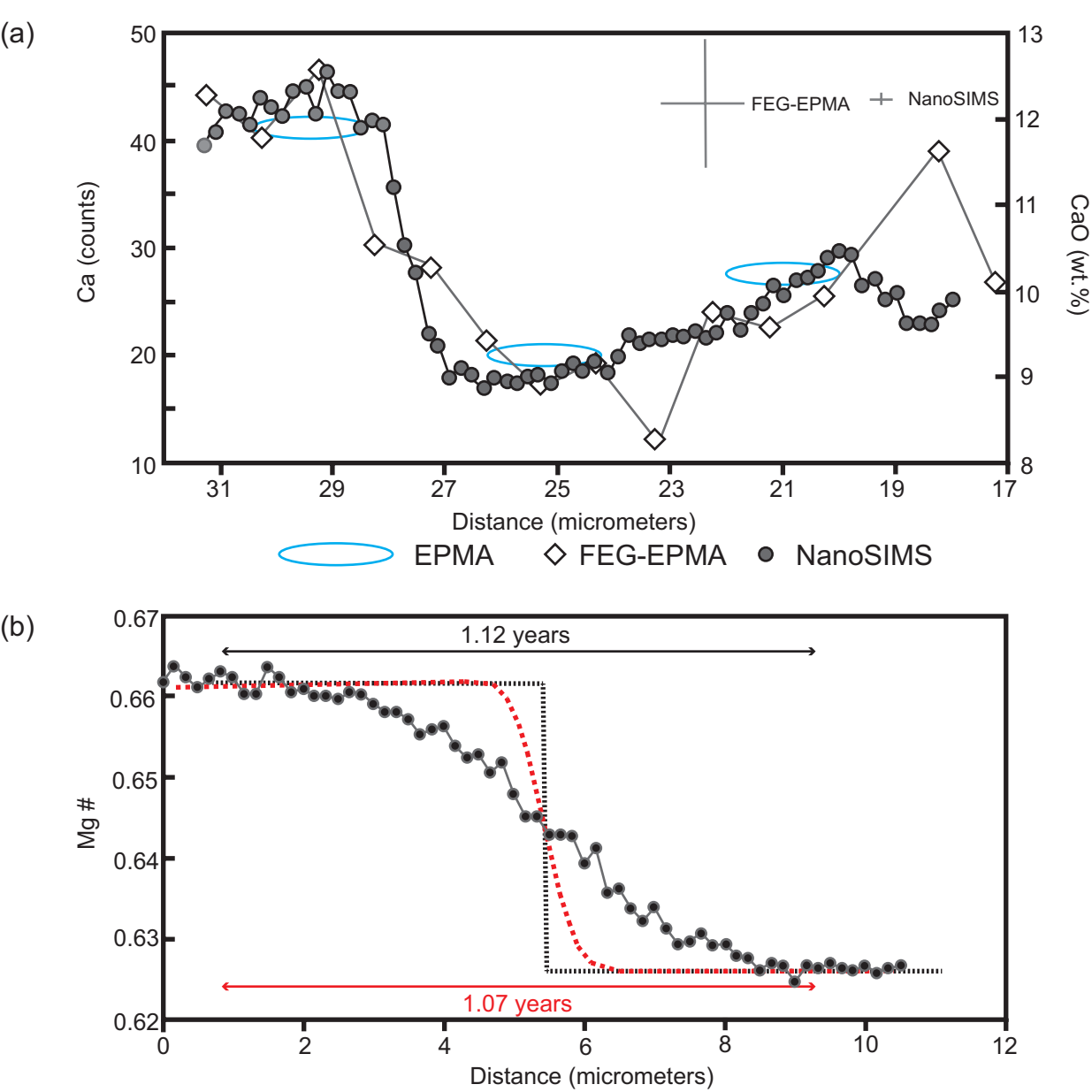
(a)
Ca (counts)
CaO (wt.%)
FEG-EPMA
NanoSIMS
Distance (micrometers)
EPMA
FEG-EPMA
NanoSIMS
(b)
Mg #
1.12 years
1.07 years
Distance (micrometers)

Table 1. Reference materials characterised at high (20kV) and low (5kV) voltage using methods as described.

	Labradorite Standard (UoB Lab001)		Labradorite (USNM 115900)		Orthopyroxene standard (internal)	
	20kV	5 kV		5 kV	**20kV**	5 kV
SiO_2	**55.63**	56.12 (1.33)	**51.25**	–	**52.54**	–
Al_2O_3	**27.90**	28.19 (0.78)	**30.91**	–	**1.39**	1.29 (0.13)^t
FeO	**0.25**	0.23^t	**0.49**	0.36 (0.03)^t	**22.52**	22.26 (0.45)^t
MgO	**–**	–	**0.14**	0.13 (0.03)^t	**22.06**	21.84 (0.71)
CaO	**10.48**	10.18 (1.50)	**13.64**	–	**0.80**	0.50 (0.08)
Na_2O	**5.41**	5.51 (0.64)	**3.45**	–	**–**	–
K_2O	**0.43**	0.37 (0.17)	**0.18**	–	**–**	–
MnO	**–**	–		–	**0.74**	–
SrO	**0.08**	–	**0.06**	0.06 (0.02)^t	**–**	–
Total	100.18	100.37 (1.36)	**100.2**		**100.05**	98.26

Standard reference values are given in bold (USNM115900, Jarosewish 1980). Reference values for the UoBLAB001 and orthopyroxene were measured at 20 kV by EPMA at Bristol as in text. 5 kV analyses are analysed by the FEG-EPMA as discussed in the text. Compositions from 5 kV analyses are based on between 6-13 points using the submicron setups specified. ^{t} Using trace element setup. Errors given in brackets are standard deviation to 2 SD.

Table 2. Minimum characteristic timescales that can be calculated for diffusion modelling at a spatial resolution of 2 μm for EPMA and 500 nm for FEG-EPMA for plagioclase crystals for a range of elements.

Element	D_x (m^2s^{-1})	Minimum temporal resolution	
		EPMA	FEG-EPMA
NaSi-CaAl	1.05×10^{-26}	12×10^6 years	7.5×10^5 years
Sr	9.22×10^{-20}	1.4 years	31 days
Mg	7.19×10^{-18}	6.4 days	9.6 hours
Ba	7.21×10^{-22}	175 years	10.9 years

Calculated from x=sqrt(Dt), where x is the distance, D the diffusion coefficient and t the time, for plagioclase crystals of An_{65} at 900°C. Diffusion coefficients for NaSi-CaAl from Grove et al., (1984); Sr from Giletti and Casserely (1994); Mg from LaTourette and Wasserburg (1998); and Ba from Cherniak, (2002).

Table 3. Comparison of high kV EPMA, low kV FEG-EPMA, NanoSIMS and TOF-SIMS, highlighting the advantages and disadvantage of each technique that are relevant to this study. Please see text for full details of each method.

	High kV EPMA	Low kV FEG-EPMA	NanoSIMS	TOF-SIMS
Minimum lateral spatial resolution*	~ 2 µm	≤ 100 nm (line) ≥ 300 nm (spot)	200 nm	500 nm
Beam diameter	~ 500nm	~ 30 nm (focused)	200 nm	500 nm
Coating material	carbon	carbon	gold	uncoated
No. elements analysed	Variable, but majors and traces tend to require different analytical protocals		5-7	All secondary ions in a single polarity
Quantification	yes	yes	no	no

* depends on analytical conditions, mineral and elements analysed. Values quoted are relevant to this study as discussed in text.

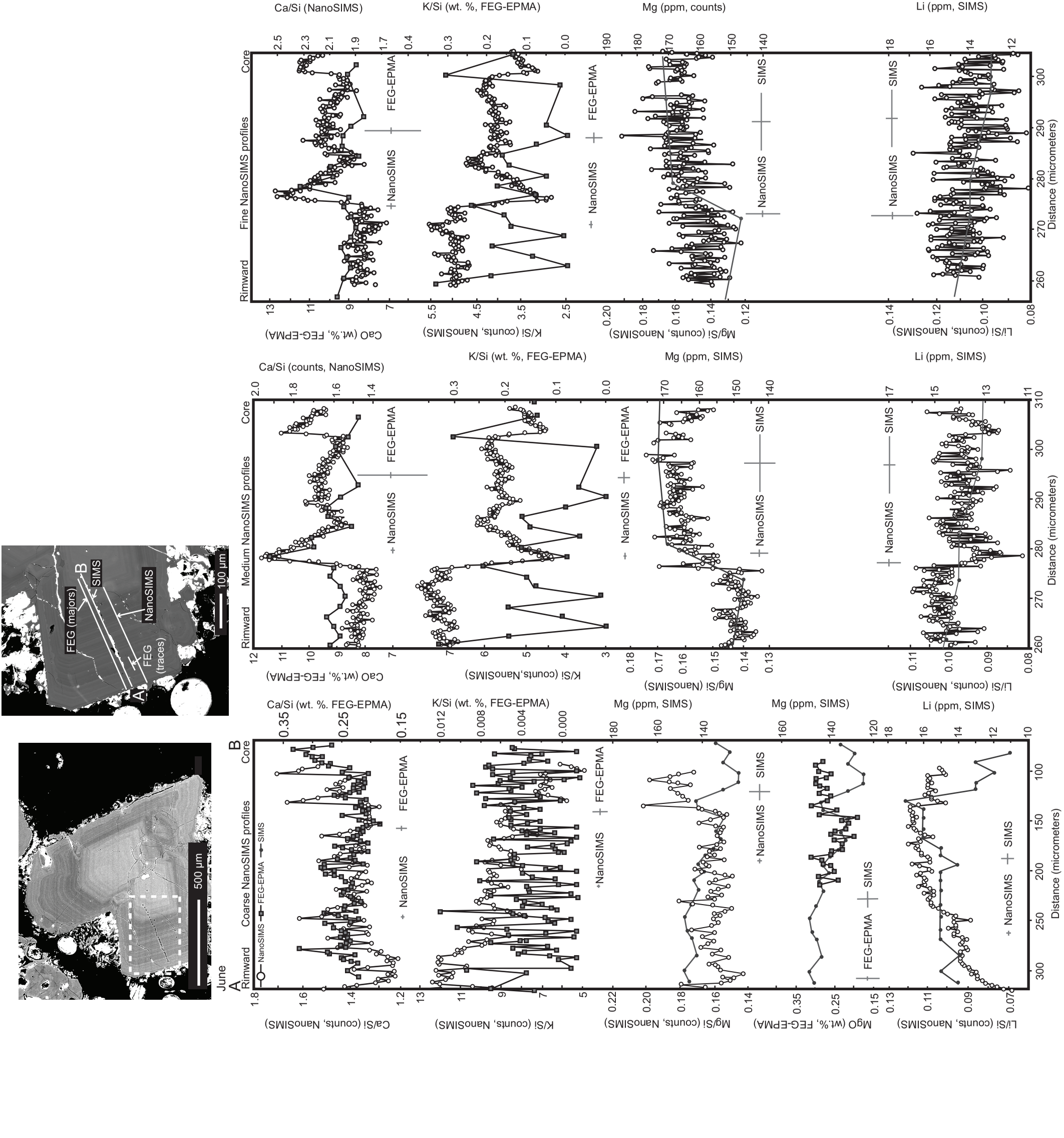
June
A
B
Rimward
Core
NanoSIMS
FEG-EPMA
SIMS
Coarse NanoSIMS profiles
Fine NanoSIMS profiles
Medium NanoSIMS profiles
Ca/Si (counts, NanoSIMS)
Ca/Si (NanoSIMS)
Ca/Si (wt. %. FEG-EPMA)
CaO (wt.%, FEG-EPMA)
K/Si (wt. %, FEG-EPMA)
K/Si (counts, NanoSIMS)
Mg (ppm, counts)
Mg (ppm, SIMS)
Mg/Si (counts, NanoSIMS)
MgO (wt.%, FEG-EPMA)
Li (ppm, SIMS)
Li/Si (counts, NanoSIMS)
Distance (micrometers)
500 µm
100 µm
FEG (majors)
FEG (traces)
SIMS
NanoSIMS

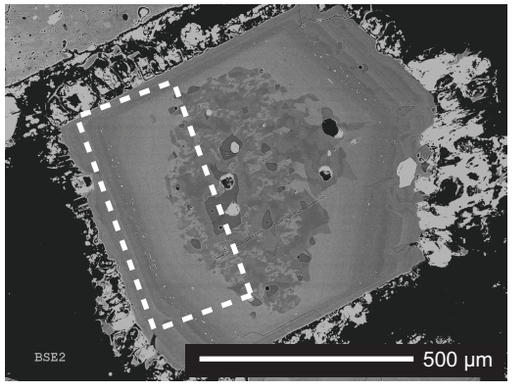
BSE2
500 µm

July

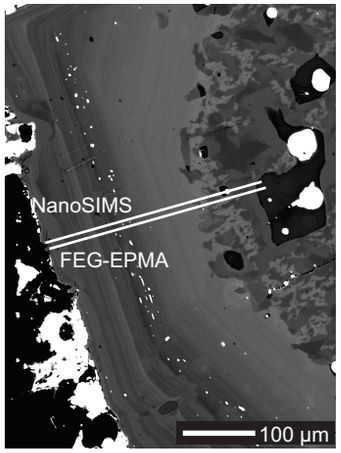
NanoSIMS
FEG-EPMA
100 µm

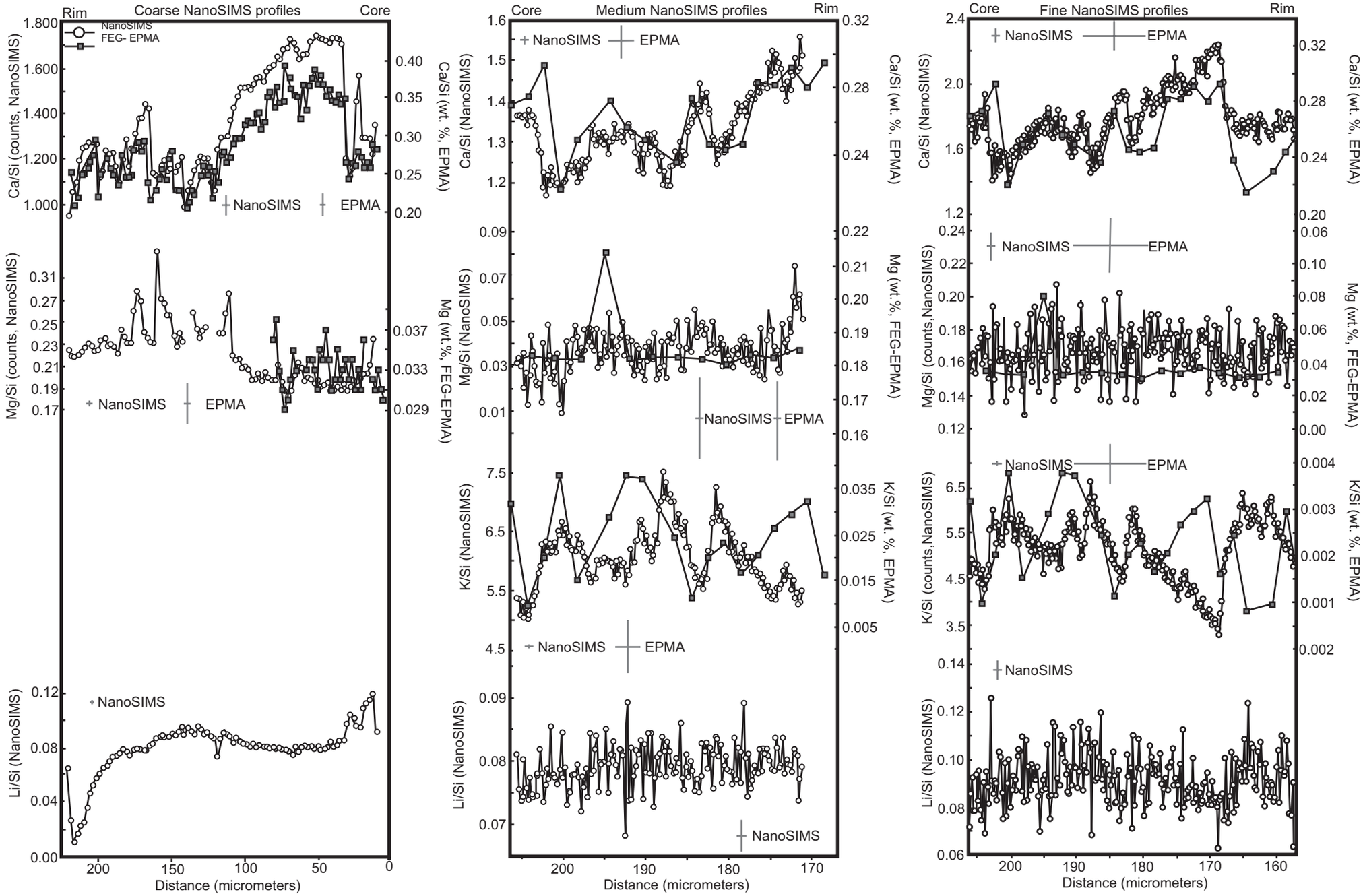
Rim
Coarse NanoSIMS profiles
Core
NanoSIMS
FEG- EPMA
Ca/Si (counts, NanoSIMS)
Ca/Si (wt. %, EPMA)
Mg/Si (counts, NanoSIMS)
Mg (wt.%, FEG-EPMA)
Li/Si (NanoSIMS)
NanoSIMS
EPMA
Distance (micrometers)
Core
Medium NanoSIMS profiles
Rim
Ca/Si (NanoSIMS)
Mg/Si (NanoSIMS)
K/Si (NanoSIMS)
K/Si (wt. %, EPMA)
Core
Fine NanoSIMS profiles
Rim
Mg/Si (counts,NanoSIMS)
K/Si (counts,NanoSIMS)

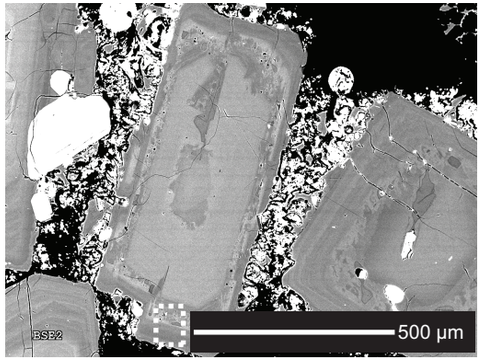
BSE2
500 µm

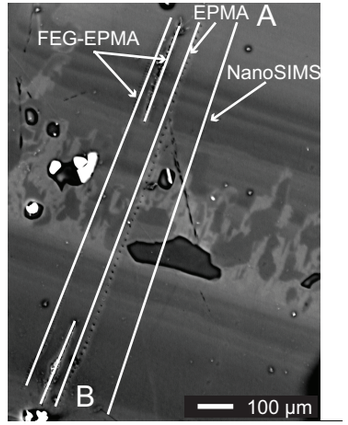
EPMA
A
FEG-EPMA
NanoSIMS
B
100 µm

Aug_7_7

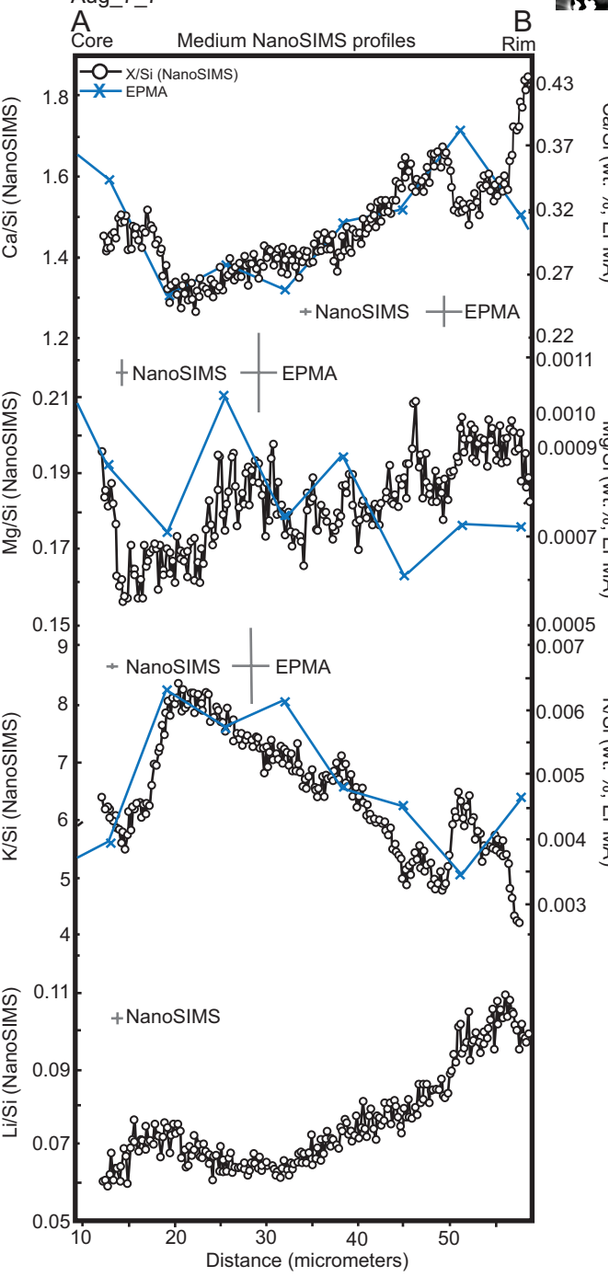
A
Core
Medium NanoSIMS profiles
B
Rim
X/Si (NanoSIMS)
EPMA
NanoSIMS
EPMA
Ca/Si (NanoSIMS)
Ca/Si (wt. %, EPMA)
Mg/Si (NanoSIMS)
Mg/Si (wt.%, EPMA)
K/Si (NanoSIMS)
K/Si (wt. %, EPMA)
Li/Si (NanoSIMS)
Distance (micrometers)

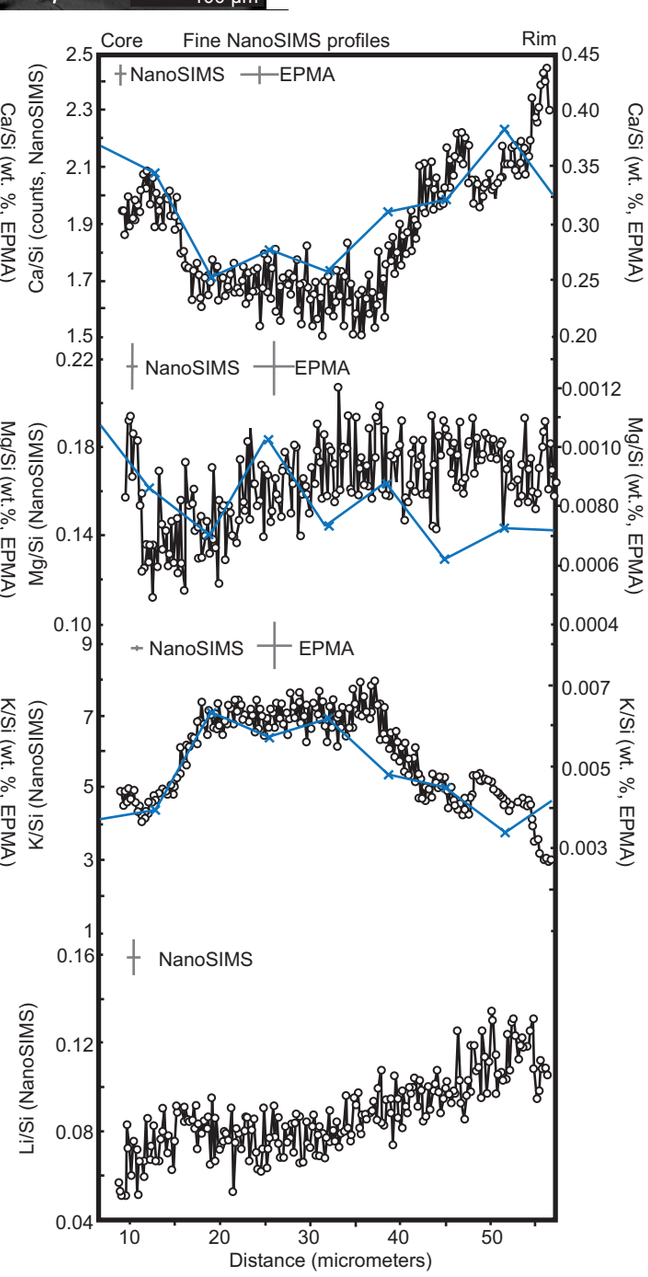
Core
Fine NanoSIMS profiles
Rim
NanoSIMS
EPMA
Ca/Si (counts, NanoSIMS)
Ca/Si (wt. %, EPMA)
Mg/Si (NanoSIMS)
Mg/Si (wt.%, EPMA)
K/Si (NanoSIMS)
K/Si (wt. %, EPMA)
Li/Si (NanoSIMS)
Distance (micrometers)

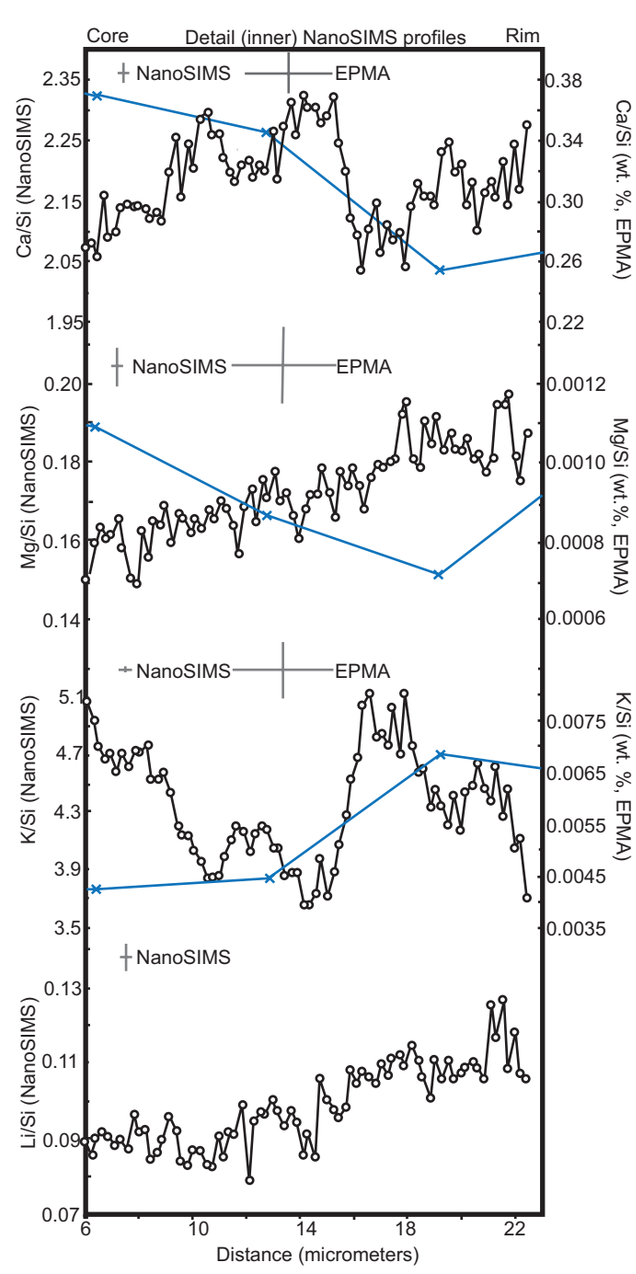
Core
Detail (inner) NanoSIMS profiles
Rim
NanoSIMS
EPMA
Ca/Si (NanoSIMS)
Ca/Si (wt. %, EPMA)
Mg/Si (NanoSIMS)
Mg/Si (wt.%, EPMA)
K/Si (NanoSIMS)
K/Si (wt. %, EPMA)
Li/Si (NanoSIMS)
Distance (micrometers)

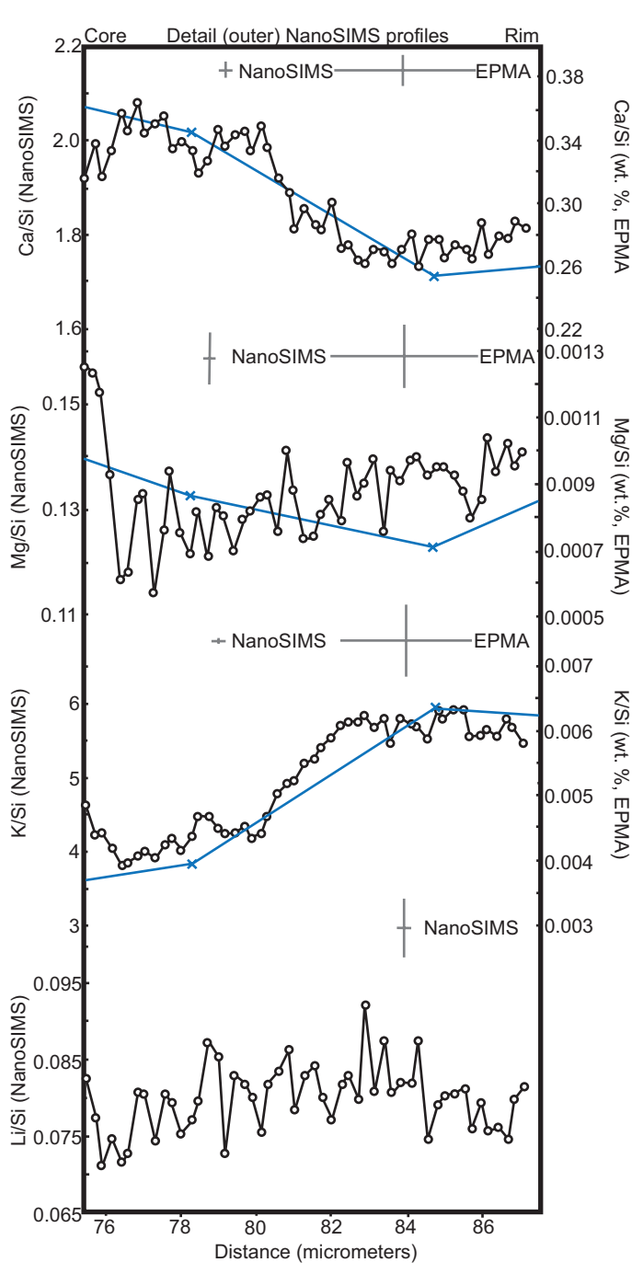
Core
Detail (outer) NanoSIMS profiles
Rim
NanoSIMS
EPMA
Ca/Si (NanoSIMS)
Ca/Si (wt. %, EPMA)
Mg/Si (NanoSIMS)
Mg/Si (wt.%, EPMA)
K/Si (NanoSIMS)
K/Si (wt. %, EPMA)
Li/Si (NanoSIMS)
Distance (micrometers)